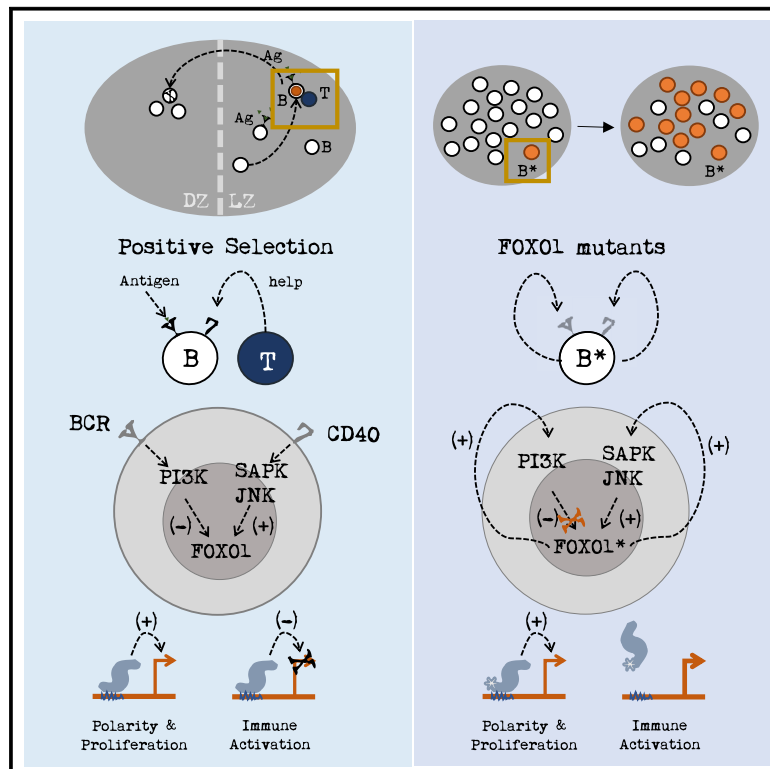# Mutations in the transcription factor FOXO1 mimic positive selection signals to promote germinal center B cell expansion and lymphomagenesis

Graphical abstract

Authors

Mark P. Roberto, Gabriele Varano, Rosa Vinas-Castells, ..., Pedro Farinha, David W. Scott, David Dominguez-Sola

Correspondence

david.dominguez-sola@mssm.edu

In brief

Mutations in the transcription factor FOXO1 are common in germinal center (GC)-derived B cell lymphomas. Roberto, Varano, et al. show that these mutations initiate concurrent gene expression and signaling programs that are characteristic of GC B cells undergoing positive selection, favoring the selective expansion of mutant B cells and lymphomagenesis.

Highlights

- FOXO1 mutations in B-NHL encode faulty proteins with altered DNA motif affinities

- Transcriptional and signaling programs of mutant GC B cells mimic positive selection

- Selective expansion of FOXO1 mutant cells during T-dependent immune responses

- Functional FOXO1 mutant gene signatures predict clinical outcomes in DLBCL

CellPress

Article

Mutations in the transcription factor FOXO1 mimic positive selection signals to promote germinal center B cell expansion and lymphomagenesis

Mark P. Roberto,[1,5,12] Gabriele Varano,[1,10,12] Rosa Vinas-Castells,[1] Antony B. Holmes,[6] Rahul Kumar,[6,11] Laura Pasqualucci,[6,7,8] Pedro Farinha,[9] David W. Scott,[9] and David Dominguez-Sola[1,2,3,4,5,13,*]

[1]Department of Oncological Sciences, Icahn School of Medicine at Mount Sinai, New York, NY 10029, USA
[2]Department of Pathology, Icahn School of Medicine at Mount Sinai, New York, NY 10029, USA
[3]Tisch Cancer Institute, Icahn School of Medicine at Mount Sinai, New York, NY 10029, USA
[4]Precision Immunology Institute, Icahn School of Medicine at Mount Sinai, New York, NY 10029, USA
[5]Graduate School of Biomedical Sciences, Icahn School of Medicine at Mount Sinai, New York, NY 10029, USA
[6]Institute for Cancer Genetics, Columbia University Medical Center, New York, NY 10032, USA
[7]Department of Pathology, Columbia University Medical Center, New York, NY 10032, USA
[8]Herbert Irving Comprehensive Cancer Center, Columbia University Medical Center, New York, NY 10032, USA
[9]Center for Lymphoid Cancer, British Columbia Cancer, Vancouver, BC V5Z 1L3, Canada
[10]Present address: Department of Translational Medicine, Laboratory for Advanced Therapy Technologies (LTTA), University of Ferrara, Ferrara, Italy
[11]Present address: Center for Brain Research, Indian Institute of Science, Bengaluru, India
[12]These authors contributed equally
[13]Lead contact
*Correspondence: david.dominguez-sola@mssm.edu
https://doi.org/10.1016/j.immuni.2021.07.009

SUMMARY

The transcription factor forkhead box O1 (FOXO1), which instructs the dark zone program to direct germinal center (GC) polarity, is typically inactivated by phosphatidylinositol 3-kinase (PI3K) signals. Here, we investigated how *FOXO1* mutations targeting this regulatory axis in GC-derived B cell non-Hodgkin lymphomas (B-NHLs) contribute to lymphomagenesis. Examination of primary B-NHL tissues revealed that *FOXO1* mutations and PI3K pathway activity were not directly correlated. Human B cell lines bearing *FOXO1* mutations exhibited hyperactivation of PI3K and Stress-activated protein kinase (SAPK)/Jun amino-terminal kinase (JNK) signaling, and increased cell survival under stress conditions as a result of alterations in FOXO1 transcriptional affinities and activation of transcriptional programs characteristic of GC-positive selection. When modeled in mice, *FOXO1* mutations conferred competitive advantage to B cells in response to key T-dependent immune signals, disrupting GC homeostasis. FOXO1 mutant transcriptional signatures were prevalent in human B-NHL and predicted poor clinical outcomes. Thus, rather than enforcing FOXO1 constitutive activity, FOXO1 mutations enable co-option of GC-positive selection programs during the pathogenesis of GC-derived lymphomas.

INTRODUCTION

Germinal centers (GCs) are transient microanatomical structures that support the positive selection and expansion of B cell clones with increasing antigen receptor affinities (Mesin et al., 2016; Victora and Nussenzweig, 2012). During this process, B cells compete to capture help from T follicular helper cells in the light zone of the GC, which is provided by strong co-stimulatory immune signals (Victora and Nussenzweig, 2012). "Affinity-selected" B cells then travel to and expand in the dark zone of the GC, where they hypermutate their antigen receptors and return to the light zone for a new round of selection. Iterations of this cycle in each GC are necessary to produce refined B cell

repertoires and ensure the success of adaptive immune responses (Mesin et al., 2016; Victora and Nussenzweig, 2012). A majority of B cell non-Hodgkin lymphomas (B-NHLs) originate from GC B cells (Basso and Dalla-Favera, 2015) and accumulate somatic genetic alterations that lead to dysregulation of signaling circuits and gene programs essential to GC physiology (Basso and Dalla-Favera, 2015; Mlynarczyk et al., 2019; Shaffer et al., 2012). Understanding the precise mechanistic contribution of these alterations to B-NHL pathogenesis is critical to define better clinical stratification and therapeutic strategies.

The transcription factor FOXO1 (forkhead box O1) coordinates gene networks defining B cell fate and transcriptional responses downstream of key immune receptors (Dengler et al., 2008; Lin
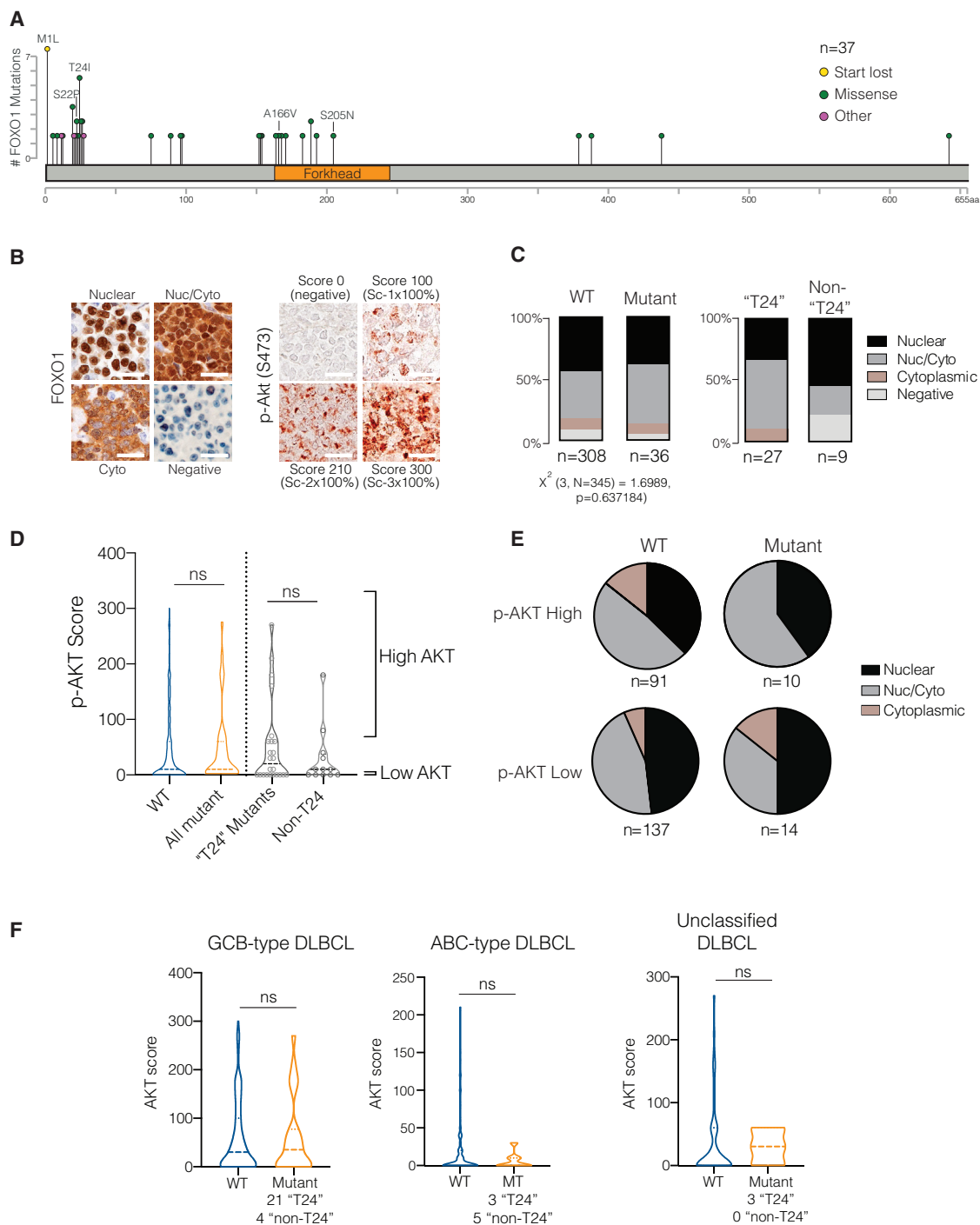
Figure 1. Correlates between FOXO1 mutations, subcellular localization, and PI3K/AKT signaling status in human DLBCL

(A) Distribution of 37 *FOXO1* mutations found in a series of 345 primary DLBCL (BCC lymphoma collection), colored by categories (Arthur et al., 2018; Ennishi et al., 2019). "Other" refers to in-frame deletions or frameshift mutations.

(B) Representative images of DLBCL samples stained for FOXO1 (left, subcellular distribution) and p-AKT S473 (right, immunohistochemical-IHC scores) via immunohistochemistry. Scale bars, 100 μm.

(C) Left: summary of FOXO1 subcellular distribution in WT or mutant FOXO1 DLBCL cases. Cases with no detectable FOXO1 protein are scored as "negative." Chi square test, not significant. Right: FOXO1 subcellular distribution in mutant cases is shown, subdivided into "T24" (mutations in M1 or R19-L27 segment) and non-"T24" mutations.

(D) p-AKT scores in WT or mutant FOXO1 patient samples stratified by FOXO1 mutation status. ns, non-significant (Mann-Whitney U test).

(legend continued on next page)

et al., 2010). FOXO1 instructs the dark zone program required for the establishment of GC polarity by controlling expression of chemokine receptors (i.e., CXCR4) and immune activation genes. These functions are critical for B cell affinity maturation (Dominguez-Sola et al., 2015; Inoue et al., 2017; Sander et al., 2015). Immune receptor signaling cascades (i.e., B cell receptor) promote AKT-mediated FOXO1 phosphorylation, nuclear export, and inactivation (Su et al., 2011; Yusuf et al., 2004). Recurrent missense somatic mutations targeting FOXO1 can be found in a significant fraction of GC-derived, aggressive variants of B-NHL (29%–54% Burkitt lymphomas, ∼10% of *de novo* and 36% relapsed or refractory diffuse large B cell lymphomas, and ∼15% transformed follicular lymphomas; Grande et al., 2019; Morin et al., 2013, 2016; Pasqualucci et al., 2014; Zhou et al., 2019). Although loss-of-function alterations in FOXO1 are found in a variety of solid tumors and in Hodgkin's lymphoma (Paik et al., 2007; Xie et al., 2012), current models suggest that in B-NHL, FOXO1 mutations are pro-oncogenic gain-of-function alleles, resulting in impaired phosphatydil-inositol 3-kinase (PI3K)/AKT-phosphorylation-mediated FOXO1 inactivation and constitutive FOXO1 signaling (Kabrani et al., 2018; Trinh et al., 2013). Moreover, the presence of FOXO1 mutations is associated with worse clinical outcomes and disease progression in some studies (Morin et al., 2016; Pasqualucci et al., 2014; Trinh et al., 2013), and FOXO1 programs can sustain lymphoma B cell survival (Kabrani et al., 2018; Trinh et al., 2013). However, the mechanistic contributions of FOXO1 mutations to altered GC physiology and links to lymphomagenesis remain poorly understood.

Here, we examined how *FOXO1* B-NHL mutations impact normal and tumoral GC B cell phenotypes. We found that these mutations encode for partially hypomorphic protein variants that mimic signaling and transcriptional features of positively selected B cells, favoring the competitive expansion of FOXO1 mutant B cells during GC responses.

RESULTS

FOXO1 mutations and PI3K/AKT signaling do not predict FOXO1 subcellular distribution in GC-derived lymphomas

To review the overall distribution and identities of *FOXO1* mutations in GC-derived, aggressive B-NHL, we compiled a comprehensive meta-analysis of publicly available series of genomics data in Diffuse Large B cell lymphoma (DLBCL) and Burkitt lymphoma (BL) (n = 2,903; Figure S1, Table S1, and references therein). Consistent across all studies and lymphoma types was the identification of a mutational hotspot (∼48% of all mutations) clustered around Arg19-Leu27, comprising a known Protein Kinase B-Akt (AKT) phosphorylation motif surrounding T24 ("T24-like"; Figure S1; Supplemental information). The predicted outcome of these missense mutations is the disruption of T24 phosphorylation and FOXO1 nuclear retention (Su et al., 2011; Van Der Heide et al., 2004).

We sought to find evidence of this notion by performing immunohistochemical analysis of a large panel (n = 345) of curated DLBCL patient samples (Arthur et al., 2018; Ennishi et al., 2019), representative of the frequency (∼10%) and distribution pattern of *FOXO1* mutations in DLBCL patients (Figures 1A and S1). We found that the patterns of FOXO1 subcellular distribution were largely equivalent in both wild-type (WT) and *FOXO1* mutant cases (Figures 1B and 1C), regardless of the presence of mutations specifically targeting the AKT site at T24, or other segments of the protein (non-T24; Figure 1C). High or low phospho-AKT (Ser473) scores—surrogates of PI3K pathway activity (Figures 1B–1D)—were equally distributed among WT, T24, and non-T24 mutant cases (Figure 1D), and no significant associations between p-AKT scores and FOXO1 localization were found (Figure 1E). In fact, similar percentages of WT or FOXO1 mutant cases were cytosolic (∼14%), including cases with T24-like mutations, suggesting that these mutations are not unequivocal predictors of FOXO1 nuclear retention. These observations were equivalent across DLBCL subtypes (Figure 1F). Overall, we found a lack of correlation between PI3K/AKT signaling status, *FOXO1* mutations, and subcellular localization, suggesting that selection of *FOXO1* mutations during lymphomagenesis cannot be explained solely by the effects of PI3K/AKT on FOXO1.

Altered signaling dictates how FOXO1 mutant proteins localize and respond to PI3K

To investigate the functional outcomes of the most prevalent B-NHL *FOXO1* mutations in B cells, we used CRISPR-Cas9-mediated gene editing to engineer isogenic mutant clones in a GCB-like DLBCL cell line (SUDHL4), which carries WT *FOXO1* alleles. We produced clones carrying p.Thr24Ile (T24I) and p.Ser22Pro (S22P) heterozygous mutations, as well as several clones carrying a p.Met1Leu (M1L) homozygous mutation, which is particularly common in GCB-like DLBCL. The M1L mutation results in a truncated protein that starts at Met71 and lacks residues 1–70, including R19-L27 (Trinh et al., 2013). Sequencing and karyotyping confirmed identity and allele balance in the resulting isogenic lines (Figures S2A and S2B).

We first analyzed the subcellular distribution of FOXO1 protein in WT and homozygous M1L isogenic SUDHL4 clones via immunofluorescence (Figures 2A and 2B). Under normal growth conditions, FOXO1 was predominantly cytosolic in WT SUDHL4 cells, although blockade of PI3K signaling with a pan-PI3K inhibitor (GDC-0941) resulted in ubiquitous FOXO1 nuclear accumulation (Figures 2A and 2B) and loss of FOXO1 phosphorylation at T24 (Figure 2C). In contrast, FOXO1 M1L mutant protein was evenly distributed between nucleus and cytosol. The cytosolic fraction of mutant protein (unphosphorylated at T24; Figure 2C) fully relocated to the nucleus upon PI3K inhibition (GDC-0941; Figures 2A and 2B), implying that M1L FOXO1 is still modulated by PI3K signaling under basal conditions. When we tested the response to B cell receptor crosslinking with anti-immunoglobulin M (IgM) and IgG antibodies—enforcing acute activation of PI3K and ERK signaling, we found that both WT and mutant

---

(E) Distribution of FOXO1 subcellular localization in patient samples according to mutational status and p-AKT score. "High" and "low" correspond to cases within the top and bottom quartiles of p-AKT scores, respectively.

(F) Quantification of p-AKT levels in patient samples with or without FOXO1 mutations, separated into DLBCL subtypes (GCB, ABC, or unclassified).

Violin plots (C–E) show median with upper and lower quartiles (Mann-Whitney U test). See also Figure S1 and Table S1.
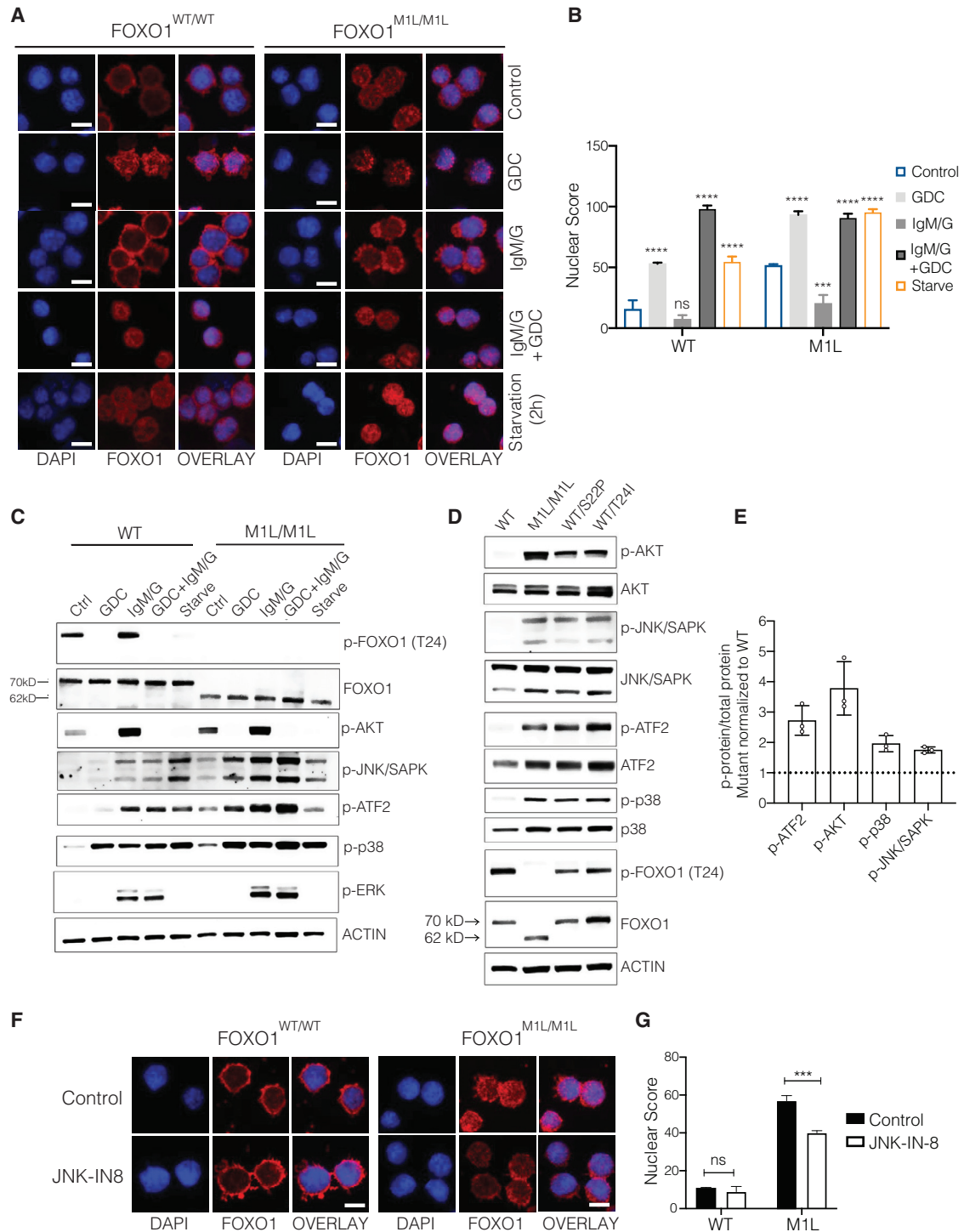
Figure 2. Signaling rewiring by FOXO1 mutants alters FOXO1 distribution in response to upstream signals

(A) Relocalization of FOXO1 proteins in WT or FOXO1 M1L/M1L isogenic SUDHL4 cells (immunofluorescence) in response to exposure to anti-IgM and IgG, PI3K inhibitor (GDC-0941), or the combination for 30 min (see STAR Methods). Starvation induced by switching cultures to Hank's balanced salt solution (HBSS) plus 1% IMDM for 2 h. Images representative of 4 to 5 experiments (two technical replicates per clone, two clones per variant, including two WT single clone control lines). Scale bar, 100 μm.

(B) Nuclear scores for FOXO1 extracts from immunofluorescence (IF) data in (A) (see STAR Methods). A minimum of 100 cells were counted for each experiment. Mean ± SD is shown.

(C) Immunoblot of FOXO1 WT or M1L SUDHL4 cells, treated as described in (A). Findings were confirmed using a WT clonal control line.

(legend continued on next page)

M1L FOXO1 protein fully relocated to the cytosol. These effects were fully blocked by addition of GDC-0941 (Figures 2A–2C; GDC). Thus, under strong PI3K signals (Figure 2C), mutant M1L FOXO1 can respond "canonically" to this pathway, independent of T24 phosphorylation. This effect is likely explained by the presence of additional AKT phosphorylation sites in FOXO1 (Ser256 and Ser319) also governing FOXO1 subcellular localization (Calnan and Brunet, 2008).

Opposite to the effects of PI3K/AKT signaling, starvation is known to trigger cellular stress responses that engage stress-associated protein kinases (JNK and p38, hereby referred to as SAPKs), silence AKT activity (Fruman et al., 2017; Wang et al., 2005), and enforce FOXO1 nuclear localization and activity (Essers et al., 2004; Huang and Tindall, 2007). In WT SUDHL4 cells, severe starvation resulted in the accumulation of FOXO1 protein in the nucleus (nuclear score ~52; Figures 2A and 2B), coinciding with loss of S473 AKT phosphorylation, activation of SAPK/JNK (p-T183/Y185) and p38 mitogen-activated protein kinase (MAPK) (p-T180/Y182) signaling, and phosphorylation of ATF2 at Thr71 (T71)—a typical consequence of JNK activation upon amino acid starvation (Chaveroux et al., 2009; Figure 2C). Starvation enforced significantly higher FOXO1 nuclear scores in FOXO1 mutant cells (score ~100; Figures 2A and 2B), despite equivalent or slightly lower levels of JNK/ATF-2 phosphorylation (Figure 2C). This difference is likely due to the addition of FOXO1 protein relocated from the cytosol to a fraction that is already nuclear in basal conditions.

Close examination of these results indicated that JNK, p38alpha, and ATF2 were abnormally phosphorylated in FOXO1 mutant (M1L) cells grown in complete medium (Figure 2C, lanes 1 and 6), concurrent with unusually high levels of AKT phosphorylation. Specific inhibition of PI3K signaling (GDC-0941) further altered this balance by abnormally magnifying SAPK (JNK/p38), particularly after BCR crosslink (Figure 2C, lanes 2–4 versus 7–9). Minor differences in p-ERK levels were also visible following BCR crosslink. Additionally, in cells recovering from starvation upon serum addition (Figure S3A), AKT phosphorylation was quickly restored in WT and mutant cells but with faster and hyperactive kinetics in mutant cells (Figure S2C, lanes 2–4 versus 5–8). Although JNK (p-JNK and p-ATF2) and p38 (p-p38) signaling quickly faded in WT cells upon serum addition, they remained stable in mutant cells (Figure S2C; 30–60 min). Phosphorylation of ribosomal protein S6 (p-S6), a surrogate of mTOR activity, did not show any measurable differences (Figure S2C). Thus, the normal balance between PI3K and SAPK/JNK signaling (Vivanco et al., 2007) is altered in FOXO1 mutant B cells.

We extended these findings to a panel of FOXO1 mutant isogenic SUDHL4 cell clones with homozygous (M1L) and het-erozygous (S22P and T24I) mutations (Figure 2D). All mutant cells showed abnormal co-hyperactivation of PI3K/AKT and SAPK signaling in basal growth conditions. In complementary experiments, reconstitution of FOXO1 null (SUDHL4, via CRISPR-Cas9) or FOXO1-depleted cells (short hairpin RNA [shRNA]; SUDHL4, SUDHL10, and OCI-LY7—all FOXO1 WT) with mutant (M1L, S22P, and T24I), but not WT, FOXO1 caused rapid co-hyperactivation of PI3K/AKT and SAPK signaling, coincident with complete (T24I) or substantial loss (S22P) of FOXO1 phosphorylation at T24 (Figures S2D and S2E). Collectively, these results indicate that acquisition of FOXO1 mutations in GC-like B cells leads to anomalous co-hyperactivation of PI3K/AKT and SAPK/JNK pathways and altered feedback signaling responses. Altering the balance between these signals by hyperactivating PI3K (see Figures 2A–2C) or pharmacological inhibition of JNK signaling restored FOXO1 M1L cytosolic localization. Particularly, specific inhibition of JNK (JNK-IN-8; Szczepankiewicz et al., 2006) led to a robust (>30%) increase in the fraction of SUDHL4 mutant cells with cytosolic FOXO1 without measurable effects on WT cells (Figure 2E), indicating that this pathway, known to enforce FOXO nuclear translocation in multiple systems (Calnan and Brunet, 2008; Wang et al., 2005), contributes to the nuclear retention of FOXO1 mutant proteins.

Hyperactivation of PI3K and SAPK in FOXO1 mutant B cells promotes resistance to stress signals

The balance between PI3K/AKT and SAPK/JNK is altered in responses to cellular stress, e.g., upon nutrient starvation, and these responses rely on FOXO1 activity (Eijkelenboom and Burgering, 2013; Fruman et al., 2017) to determine cell fate and survival (Fulda et al., 2010; Hotamisligil and Davis, 2016). Hence, to test the impact of altered signaling in FOXO1 mutant cells, we used a co-culture system evaluating cellular fitness under starvation (Figure 3A). In these assays, WT cells were gradually depleted upon activation of caspase-3 (6 h) and eventually died after prolonged starvation (48 h; Figures 3B, 3C, and S3A–S3C), but this response that was clearly delayed in FOXO1 mutant cells (Figures 3D, 3E, S3B, and S3C). Because isolated cultures of WT or mutant cells showed similar differences in caspase-3 activation (6 h; Figures S3D and S3E), we concluded that the phenotype depended on cell intrinsic mechanisms. The dynamics of AKT phosphorylation and JNK/SAPK (and p38alpha) signaling in response to starvation were also altered in mutant cells (Figure S3F), suggesting a disruption of normal feedback regulation. Notably, although inhibition of either PI3K or SAPK/JNK had minor but statistically significant effects on FOXO1 mutant B cells, their combined inhibition increased caspase-3 activation to levels equivalent to those observed in

---

(D) Immunoblot analysis of WT or mutant FOXO1 isogenic SUDHL4 CRISPR clones (homozygous M1L/M1L; heterozygous WT/S22P and WT/T24I), cultured in Iscove's Modified Dulbecco's Medium (IMDM) with 10% fetal bovine serum (FBS). Findings were validated using multiple WT single clone controls.

(E) Densitometry analysis of (D). Phosphorylated protein levels normalized to total protein, and data from all three mutant cell lines normalized to FOXO1 levels in WT cells. See also Figure S3.

(F) Immunofluorescence analysis of FOXO1 protein distribution in WT or FOXO1 M1L/M1L isogenic SUDHL4 cells in response to JNK-IN8 (1 μM; 30 min). Images representative of 4 to 5 experiments are shown (two technical replicates per clone, two clones per variant, including two WT single clone control lines). Scale bar, 10 μm.

(G) Summary of FOXO1 nuclear scores (as per immunofluorescence in F; see STAR Methods). A minimum of 100 cells were counted for each experiment. Mean ± SD is shown.

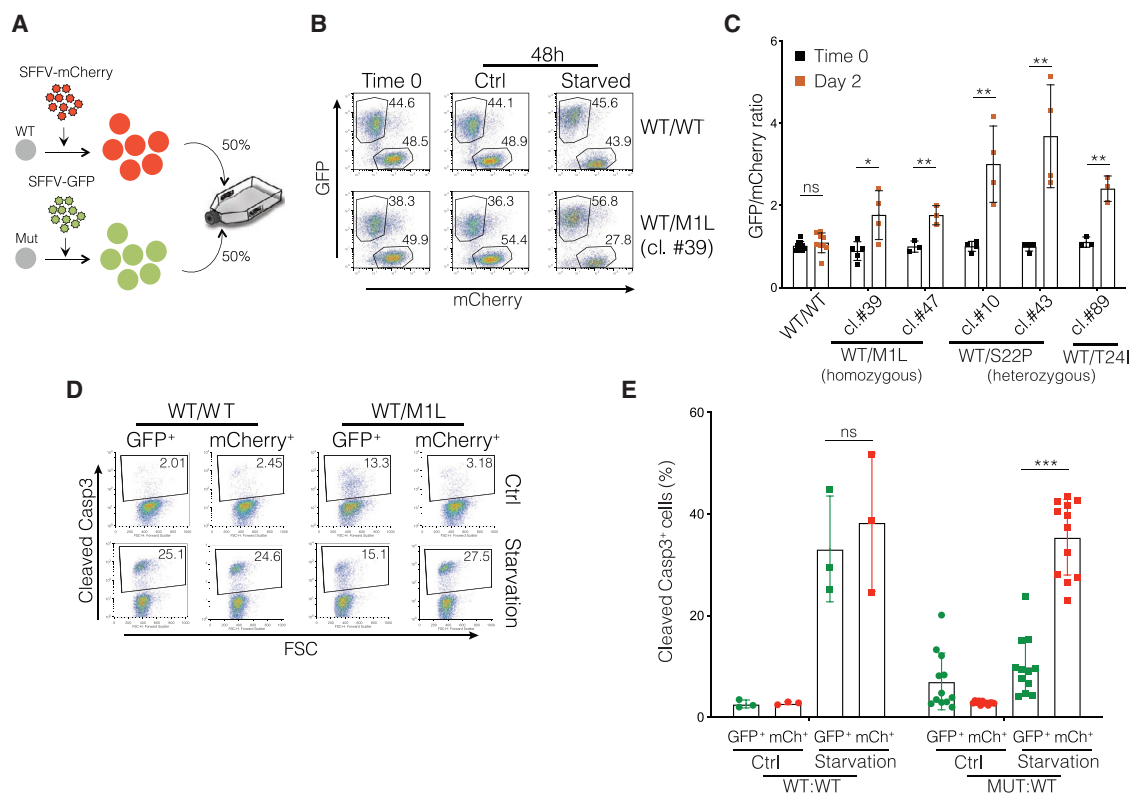Unpaired t test: *p < 0.05; **p < 0.01; ***p < 0.001.

Figure 3. Abnormal hyperactivation of PI3K and SAPK/JNK signaling confers increased resistance to starvation-induced apoptosis in FOXO1 mutant SUDHL4 cells

(A) Schematics of cell competition assay: CRISPR-edited SUDHL4 clones were transduced with lentiviral particles encoding mCherry (wild-type cells [WT]) or GFP (mutant cells [Mut]). GFP+ and mCherry+ cells were mixed in 1:1 ratio and co-cultured in full medium (Ctrl, IMDM with 10% FBS) or starvation medium (HBSS with 1% IMDM). GFP:mCherry ratios were determined by flow cytometry. A WT (mCherry):WT(GFP) co-culture was used as control.

(B) Representative flow cytometry analysis of SUDHL4 WT:M1L co-cultures in full medium or under starvation (48 h). See also Figure S4.

(C) Summary of results of co-culture experiments. Ratios between GFP+ over mCherry+ cells are shown. Each dot represents one independent experiment. WT(GFP+):WT(mCherry+) co-cultures were used as control. Average ± SD is shown. Unpaired t test: ns, not significant;*p < 0.05; **p < 0.01; ***p < 0.001.

(D) Representative flow cytometry analysis of caspase-3 activation in FOXO1 WT and mutant SUDHL4 clones (6 h co-culture). Results from multiple clones, including two individual WT single clone-derived cells, are summarized in (E). See also Figure S4.

(E) Summary of data from (D). Each dot represents one independent experiment. Mean ± SD is shown (Student's t test, two-tailed). Unpaired t test: ns, not significant; *p < 0.05; **p < 0.01; ***p < 0.001.

WT cells upon severe starvation (Figures S3G–S3I). Thus, hyperactive PI3K/JNK signals provided FOXO1 mutant cells with a functional advantage under cellular stress.

Dysregulated transcriptional repertoires hyperactivate PI3K/SAPK in FOXO1 mutant B cells

To further understand the mechanistic basis for these functional differences, we analyzed the transcriptional programs (RNA sequencing [RNA-seq]) and chromatin distribution (chromatin immunoprecipitation sequencing [ChIP-seq]) of WT and mutant FOXO1 proteins in isogenic SUDHL4 clones. Despite apparent differences in subcellular distribution (Figures 2A and 2B), both protein variants had low levels of chromatin association in basal growth conditions. Brief starvation induced selective recruitment of comparable amounts of WT and mutant (M1L) FOXO1 proteins to chromatin (Figure 4A), suggesting that any functional differences could be of qualitative nature. We used these specific conditions (brief starvation) to survey FOXO1 genomic binding (ChIP-seq).

Overall, WT and mutant (M1L) FOXO1 proteins showed comparable genome-wide distribution, with a majority of bound regions located at regulatory elements within gene bodies (~49%; i.e., intronic regions) and intergenic regions (~31% of peaks). Only a small fraction of protein was found within promoter regions (~19%–20%; Figure S4A). This pattern resembled that of FOXO1 in normal human GC B cells (Dominguez-Sola et al., 2015). Although the repertoires were largely overlapping (4,113 peaks; ~88% of FOXO1 M1L bound peaks; see Table S2), a sizeable number of regions were specific to each FOXO1 variant (2,818 WT-only peaks or ~33% of all WT bound regions; 564 mutant-only peaks or 12% of bound regions; Figure 4B). Equal read densities at overlapping regions (4,113 common peaks; Figure S4B) confirmed this notion. A majority of these differential regions were exclusive to WT FOXO1 (~80% of all differential peaks) and showed marked reductions in bound FOXO1 mutant protein (~2-fold average loss; 35 versus 65; arbitrary read units), suggesting that these may in effect represent low-affinity sites (Figure 4C). Common-bound regions were
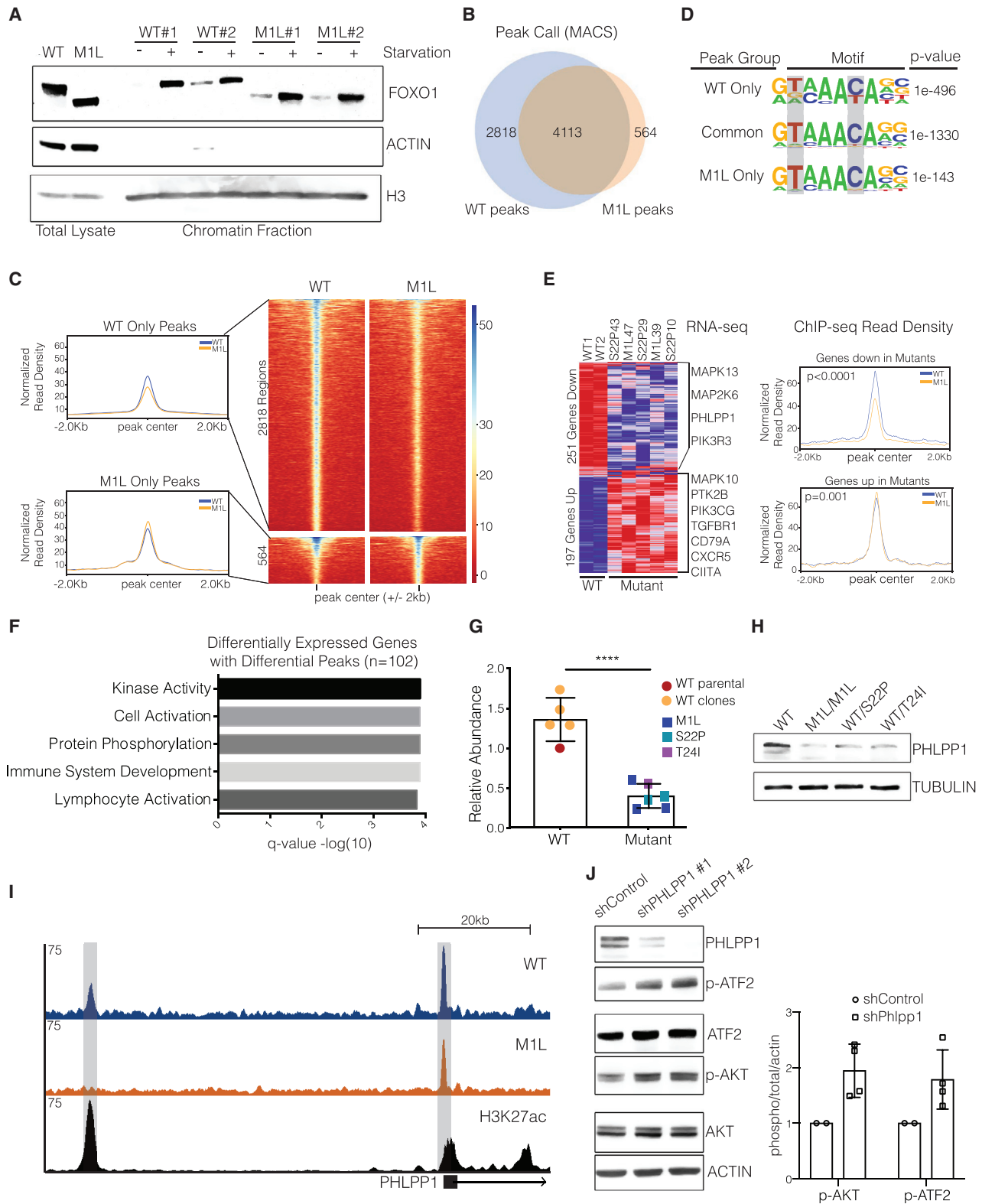
Figure 4. Defective mutant FOXO1 transcriptional repertoires dysregulate signal transduction pathways in GC B cells

(A) Immunoblot analysis in chromatin-enriched fractions of WT or M1L mutant SUDHL4 isogenic clones grown in complete medium or upon starvation (2 h). Total lysates (first two lanes) are included for reference. Result is representative of 2 independent experiments, validated using a single-cell WT clone.

(legend continued on next page)

typically enriched in a high-affinity canonical Forkhead/FOXO1 consensus motif (GTAAACA or TGTTTAC; p = 1E−1,330; Furuyama et al., 2000; Figure 4D), and WT and mutant FOXO1 proteins showed equivalent transactivation potencies when bound to this site (Figure S4C). In contrast, regions preferentially bound by mutant M1L FOXO1 appeared to have a much stricter sequence requirement, especially at certain nucleotide positions otherwise tolerated by WT FOXO1 (GTAAACA; p = 1E−143; Figure 4D) at what may constitute lower affinity sites.

We next performed RNA-seq analyses in cells grown under basal conditions, aiming to capture gene expression differences underlying the signaling features of FOXO1 mutant cells. Using supervised analysis, we identified 448 genes differentially expressed between WT and mutant SUDHL4 B cells (251 up in WT, 197 up in mutants; DESeq2 p adj < 0.05; Figure 4E; Table S3). Differences in gene expression were highly correlated with differences in chromatin occupancy, defined by statistically significant differences in FOXO1 ChIP-seq read densities at associated regulatory regions (p < 1E−4 and p < 1E−3, respectively; Kolmogorov-Smirnov (KS) test; Figure 4E, right panels).

We then applied diverse pathway analysis tools to first interrogate the list of genes differentially expressed and bound by WT or mutant FOXO1 proteins (102 genes; ~23% of all differentially expressed genes; Table S3). This list was significantly enriched in genes encoding proteins in kinase signaling pathways, particularly PI3K and SAPK/JNK (Table S3; Figures 4E and 4F), typically co-opted by B-cell-receptor- and cytokine-mediated signaling pathways. Among all signaling genes, the pleckstrin homology (PH) domain and leucine rich repeat protein phosphatase 1 gene (PHLPP1) stood out due to its reported role in the control of PI3K signaling and activity as a tumor suppressor (Chen et al., 2011). PHLPP1 belongs to the serine/threonine phosphatase family of isoenzymes (PHLPP1 and PHLPP2), and it can directly dephosphorylate and inactivate AKT to suppress the PI3K pathway (Baffi et al., 2021; Brognard et al., 2007; Gao et al., 2005). In FOXO1 mutant SUDHL4 isogenic B cells, PHLPP1 mRNA and protein expression were reduced >50%, regardless of mutation identity or allele dosage (Figures 4G and 4H). Reduced PHLPP1 expression coincided with the loss of FOXO1 binding at a distal regulatory element (putative

enhancer) located ~60 kb upstream of the PHLPP1 gene promoter (Figure 4I). PHLPP1 depletion in SUDHL4 B cells via RNA interference resulted in reproducible increases in AKT (Ser473) and ATF2 (Thr71) phosphorylation, indicative of hyperactivation of PI3K and SAPK/JNK pathways (Figure 4J), which is consistent with previous studies (Baffi et al., 2021). These observations suggest a transcriptional basis for the concurrent hyperactivation of PI3K and SAPK/JNK signaling in FOXO1 mutant B cells. Transcriptional deregulation of additional genes encoding PI3K and SAPK pathways components (Figure 4E; Table S3) could also contribute to this state. Thus, an important consequence of mutant FOXO1 activity is the transcriptional rewiring of cellular signaling (PI3K and SAPK/JNK) in B cells.

Constitutive activation of GC-positive selection programs in FOXO1 mutant B cells

Among all 448 differentially expressed genes, we found enriched signatures related to cell death (Figure 5A; Table S3), consistent with the delay in caspase-3 activation observed in mutant cells under severe starvation (Figures 3 and S3). The largest enrichments, however, corresponded to gene signatures related to regulation of immune responses, immune activation, and signal transduction (Figure 5A; Table S3)—including key genes and gene modules involved in antigen processing and presentation (CD74, CIITA, and multiple histocompatibility leukocyte antigen [HLA] genes), interferon and cytokine-chemokine signaling (e.g., CXCR5), and ICOS/ICOSL signaling (e.g., ICOSLG; Table S3). Gene sets related to CD40 and B cell receptor (BCR) signaling were particularly co-enriched (Figure 5B; Table S3), as we could confirm using additional reference datasets (Basso et al., 2004; Figures 5B and 5C).

CD40 and BCR initiate non-overlapping gene expression programs in GC B cells (Basso et al., 2004), as well as non-redundant signaling cascades (Luo et al., 2018), including PI3K/AKT and SAPK/JNK (Berberich et al., 1996; Gallagher et al., 2007; Li et al., 1996; Sakata et al., 1995). Consistent with previous studies (Luo et al., 2018), we found that activation of BCR and CD40 in SUDHL4 cells engaged separate signaling modules: although PI3K (i.e., p-AKT) and ERK (p-ERK) were strictly dependent on BCR stimulation, CD40 initiated signals through the canonical nuclear factor κB (NF-κB) pathway and SAPK/JNK

(B) Overlap between ChIP-seq peaks (MACS2; cutoff p < 10⁻⁵) found in WT or M1L FOXO1 SUDHL4 cells. Overlap was determined using the HOMER mergePeaks function. See also Figure S5A and Table S2.

(C) The heatmaps depict sequencing read densities for FOXO1 WT and M1L unique ChIP-seq peaks, centered around peak centers, as determined through the HOMER mergePeaks function. See also Figure S5B and Table S2.

(D) Most significant enriched motifs in WT only, M1L only, or common peak regions, as defined by de novo motif enrichment (findMotifsGenome function in HOMER). See also Table S2.

(E) Left: comparative RNA-seq analysis of FOXO1 WT (n = 2) and mutant (n = 5) SUDHL4 clones (448 differentially expressed genes; DESeq2, p adj < 0.05). Right: normalized ChIP-seq read densities for FOXO1 proteins in peaks corresponding to differentially expressed genes are shown. p values were calculated using Kolmogorov-Smirnov test. See also Table S3.

(F) Gene Ontology analysis (hypergeometric distribution test, Investigate Gene Set tool, MSigDB) of genes both differentially expressed and bound when comparing WT and FOXO1 M1L cells (n = 102). See also Table S3.

(G) qPCR data for PHLPP1 mRNA expression in WT parental line (n = 1), WT single clone-derived lines (n = 4), and mutant (n = 6) FOXO1 SUDHL4 cells cultured in 10% FBS (p < 0.0001; unpaired; two-tailed Student's t test). Equivalent results were observed upon serum starvation (data not shown).

(H) Immunoblot for PHLPP1 protein in WT and mutant FOXO1 SUDHL4 cell lysates, cultured in full media (10% FBS).

(I) ChIP-seq tracks from WT or M1L FOXO1 proteins at the PHLPP1 gene locus. Read density tracks from pooled replicates are shown (n = 2 WT; n = 2 M1L). y axis shows reads per kilobase per million. The H3K27ac ChIP-seq track (SUDHL4 cells) is from GEO: GSE132365.

(J) Left: immunoblot analysis of WT SUDHL4 cells 72 h post-dox induction of non-targeting and PHLPP1-specific shRNAs. Blot representative of two independent experiments is shown. Right: densitometry quantification is shown. Phosphorylated protein in PHLPP1 knockdown cells normalized to levels in control cells.
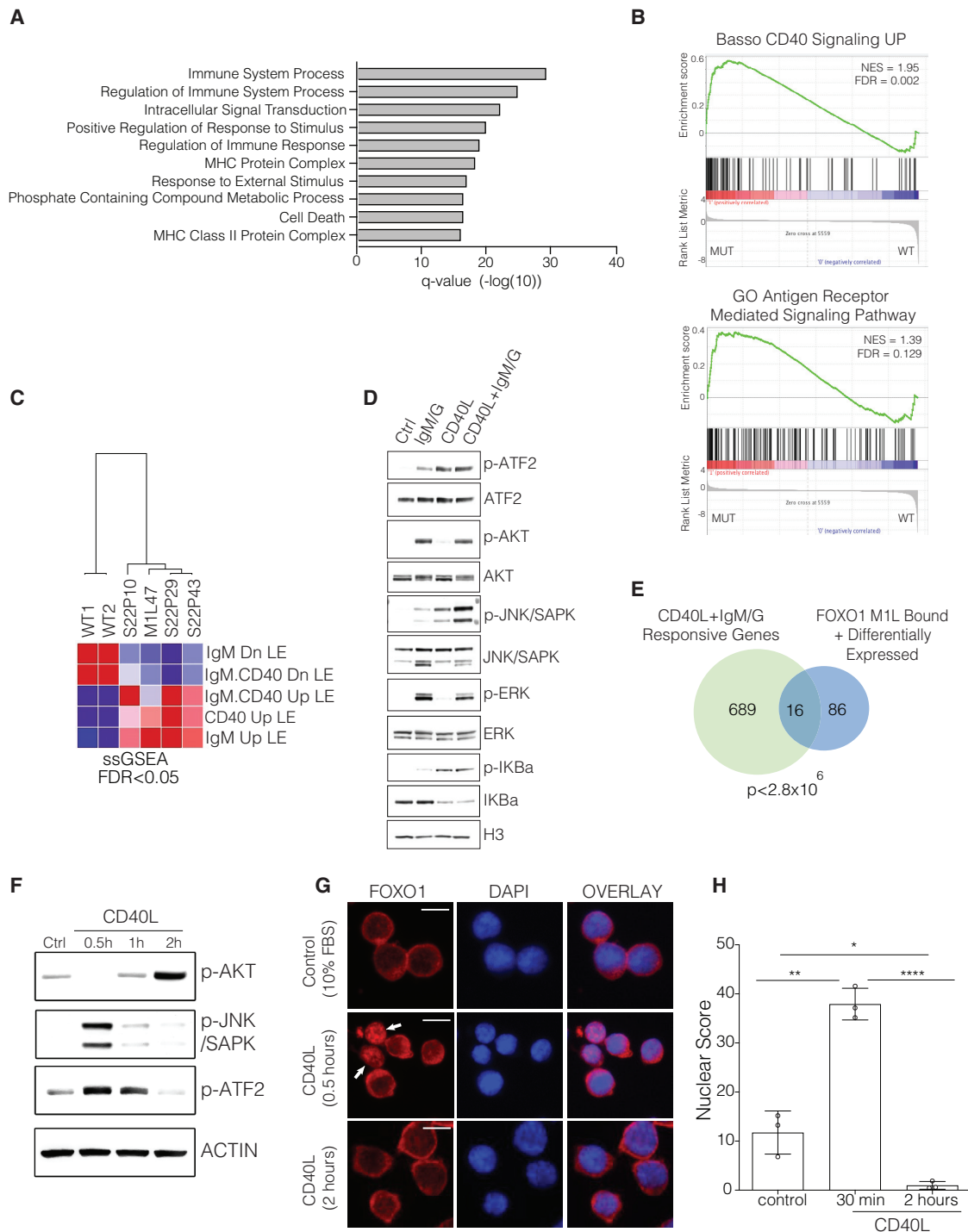
Figure 5. FOXO1 mutants mimic positive selection programs and CD40/BCR activation in GC B cells

(A) Gene ontology analysis of 448 genes differentially expressed (DESeq2, p adj < 0.05) between WT and mutant FOXO1 SUDHL4 cells. Top 10 gene ontologies are shown (hypergeometric distribution, *Investigate Gene Set* tool, MSigDB). See also Table S3.

(B) Enrichment plots (gene set enrichment analysis [GSEA]) for CD40 and antigen receptor (BCR) gene sets in FOXO1 mutant SUDHL4 cells (see also Table S3).

(C) Heatmap showing results from single-sample GSEA (ssGSEA) on WT and mutant FOXO1 SUDHL4 cells, upon interrogating leading edge (LE) genes related to IgM, CD40, or IgM+CD40 stimulation in Ramos cells (Basso et al., 2004) and enriched upon treatment of parental SUDHL4 cells with CD40L and anti-IgM and IgG antibody (Table S3).

(D) Immunoblot analysis of SUDHL4 cells stimulated with anti-IgM and IgG, CD40 ligand, or both for 30 min.

(E) Venn diagram showing overlap of genes differentially expressed in SUDHL4 cells after stimulation with CD40L and anti-IgM and genes bound by FOXO1 and differentially expressed in FOXO1 WT versus mutant SUDHL4 cells (p value, hypergeometric distribution test). See also Table S3.

(legend continued on next page)

(30 min; Figure 5D). SAPK/JNK phosphorylation was maximal when CD40 and BCR were co-engaged, indicating a strong (not additive) functional synergy. Thus, concurrent hyperactivation of SAPK/JNK and AKT phosphorylation, analogous to that seen in FOXO1 mutant SUDHL4 B cells, only occurred upon BCR and CD40 co-stimulation. The transcriptional responses to BCR and CD40 co-stimulation in SUDHL4 cells (Table S3) also significantly overlapped with those driven by acquisition of FOXO1 mutations (Figure 5E).

Although FOXO1 is a major component of the BCR signaling pathway (Rickert, 2013; Srinivasan et al., 2009; Su et al., 2011), no current reports establish a direct participation of FOXO1 in CD40 signaling. To test this possibility, we monitored the response of SUDHL4 cells to recombinant CD40 ligand (CD40L) over time (Figures 5F–5H). CD40 ligation triggered rapid and robust activation of SAPK/JNK signaling, which subsided after 2 h when PI3K signaling became predominant (Figure 5F). Notably, the "transition" from SAPK to PI3K signaling paralleled changes in FOXO1 subcellular localization, which quickly accumulated in the nucleus early after CD40 activation (30 min; ~35% of cells), coinciding with a peak in SAPK/JNK activity, and subsequently returned to the cytosol under high PI3K and low SAPK/JNK activity (Figures 5G and 5H). Thus, CD40 signaling can also directly influence FOXO1 subcellular localization, associated with temporal oscillations in SAPK/JNK and PI3K/AKT signaling.

Ongoing CD40+BCR signaling and immune activation programs identify light zone GC B cells undergoing positive selection (Ersching et al., 2017; Victora et al., 2010), detectable as MYC+ GC B cells in reporter mice (Calado et al., 2012; Dominguez-Sola et al., 2012; Ersching et al., 2017; Huang et al., 2008) or traceable upon targeted antigen delivery via the surface lectin DEC-205 (Ersching et al., 2017; Victora et al., 2010). We found that a vast majority of gene sets associated to positive selection in normal mouse GC B cells isolated with these strategies were also differentially enriched in SUDHL4 FOXO1 mutant cells (Figures S5A and S5B; Table S3). In parallel, biochemical (Figure S5C) and immunofluorescence (Figure S5D) analyses showed that SAPK/JNK and PI3K/AKT signaling were co-activated in light-zone GC B cells. A small number of these cells contained particularly high levels of SAPK/JNK activation (high p-ATF2 T71). In mice, increased levels of active SAPK (p-JNK and p-ATF2) and PI3K signaling (p-AKT) were detectable in MYC+ (GFP+; positively selected) cells, concurrent with markers of active mTOR signaling (Figures S5E and S5F), which is typically upregulated upon positive selection (Ersching et al., 2017). Thus, SAPK/JNK and PI3K/AKT signaling are co-activated upon positive selection during normal GC responses. Collectively, all these results indicate that the phenotypic features of FOXO1 mutant B cells—gene expression signatures and signaling milieu—mimic those of canonical GC B cell responses to positive selection.

Hypersensitivity of FOXO1 mutant mouse B cells to T-dependent, positive selection signals

To understand the significance of our findings in the context of normal B cell responses, we used CRISPR-Cas9 gene editing to engineer a mouse model where a M1L mutation was introduced in the first coding exon of the murine *Foxo1* locus (Figure S6A; STAR Methods). As seen in human DLBCL, this M1L mutation resulted in a truncated protein expressed at levels equivalent to those of WT Foxo1 (Figure S6B). *Foxo1* is indispensable for early B cell development and peripheral immune function in mice (Dengler et al., 2008). In *Foxo1*[M1L] mice, early B cell development in the bone marrow was largely normal, with only a minor but significant reduction in the percentage of mature B cells (55% versus 49%; p < 0.05; Figure S6C) and changes in the relative frequencies of splenic T1, T2, and T3 transitional B cells (Figure S6D), which could explain the small reduction in mature B cells. The relative percentages of follicular, transitional, and marginal zone B cells were equivalent to those in WT littermates (Figure S6E).

To determine the functional impact of *Foxo1* mutations in mature B cells, we first tested the response to *ex vivo* CD40 and BCR stimulation (Figures 6A and 6B), because these two programs appeared to be constitutively active in human FOXO1 mutant B cells (Figure 5). Stimulation of mouse splenic B cells with low concentrations of an activating anti-CD40 antibody (clone HM40-3) and interleukin-4 (IL-4) to mimic T cell help showed that a larger fraction of mutant B cells started proliferation and went through additional rounds of cell division (1.5- to 2-fold increase in division index versus WT B cells; Figures 6A and 6B). *Foxo1* mutant B cells also outperformed WT B cells in response to B cell receptor activation via crosslinking with limiting amounts of anti-IgM and IgG antibodies plus IL-4 (Figures 6A and 6B). Minor but additive effects were achieved when we combined anti-CD40 and anti-IgM and IgG. Responses to CD40, BCR, and IL-4 appeared to be proportional to allele dosage (Figures 6A and 6B). In contrast, no differences were detected when we exposed B cells to T-independent cues (Figures 6C and 6D) engaging Toll-like receptor signaling (Chaplin et al., 2011; Ogata et al., 2000). Thus, *Foxo1* mutant B cells outperform WT B cells in response to subthreshold levels of antigen receptor and T-dependent immune signals.

Competitive advantage and expansion of Foxo1[M1L] mutant B cells during GC responses and early lymphomagenesis

Entry and expansion of B cells in GCs relies on their ability to "capture" positive selection signals (Mesin et al., 2016; Victora and Mesin, 2014), delivered through a combination of immune cues, including BCR and CD40. To determine how the phenotypic differences detected in *ex vivo* assays translated *in vivo*, we first immunized *Foxo1*[M1L] and WT mice to induce polyclonal GC responses. Notably, the percentage of GC B cells in the

---

(F) Immunoblot analysis of SUDHL4 cells stimulated with CD40L. Lysates from SUDHL4 cells cultured in complete growth medium are used as control. Data are representative of 3 independent experiments, validated using a single clone-derived WT SUDHL4 cell lines.

(G) Immunofluorescence analysis of FOXO1 subcellular distribution in WT SUDHL4 cells in response to CD40L. White arrows point at cells with nuclear FOXO1. Representative images are shown (3–5 independent experiments), including validation with an isogenic WT SUDHL4 clonal line. Scale bar, 10 μm.

(H) Quantification of immunofluorescence analysis (F). Data are displayed as the percentage of cells with nuclear FOXO1. A minimum of 100 cells were counted per replicate (n = 3–5). Unpaired t test: *p < 0.05; **p < 0.01; ****p < 0.0001.
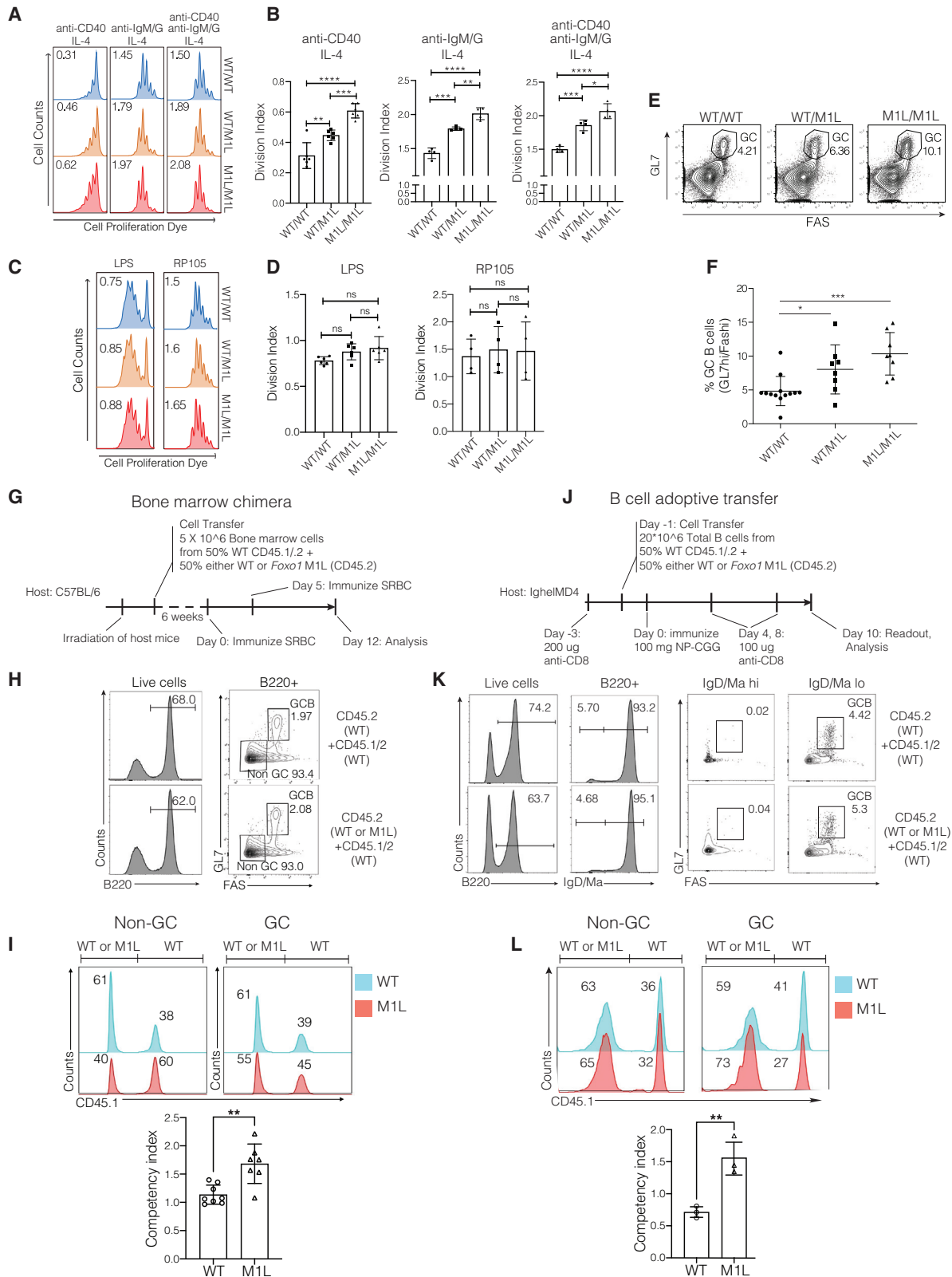
Figure 6. Enhanced sensitivity to T-dependent immune signals and competitive expansion of *Foxo1* M1L mutant B cells during GC responses

(A) Representative flow cytometry analysis of cell proliferation in *Foxo1*[WT/WT], *Foxo1*[WT/M1L], and *Foxo1*[M1L/M1L] B cells stimulated for 72 h with different cytokine plus agonist antibody combinations (see also STAR Methods for details). Division indices are shown in the top left corner of each graph.

(legend continued on next page)

spleen was higher in *Foxo1*[M1L] mice (1.5-fold in heterozygous, p < 0.02; 2.5-fold in homozygous mice, p = 1e−3; Figures 6E and 6F), consistent with increases in the number and size of GCs (∼1.5-fold; Figures S6F and S6G). *Foxo1* mutant GCs also showed altered dark-to-light zone ratios, with a relative expansion of the dark zone B cell compartment (2:1 to 3:1 ratio; WT versus mutant, respectively; p < 0.01; Figure S6H). This observation was consistent with the known role of Foxo1 in controlling light to dark zone transit in the GC (Dominguez-Sola et al., 2015; Inoue et al., 2017; Sander et al., 2015) and the abnormal expansion of *Foxo1* mutant GCs. We did not find significant differences in the total number of T follicular helper (Tfh) cells (Figures S6I and S6J).

To understand whether the phenotypes of *Foxo1*[M1L] B cells translated in competitive advantages *in vivo*, we produced mixed bone marrow chimeras in which we combined equal numbers of WT (CD45.1/2) and either wild-type (control) or *Foxo1*[M1L] CD45.2 donor bone marrow cells (Figure 6G). We then immunized all recipient mice and determined the relative abundance of CD45.1/2 and CD45.2 cells in both GC and non-GC B cell pools ("competitive competency"; see STAR Methods for details; Figure 6H). By day 12 post-immunization, homozygous *Foxo1*[M1L] B cells had effectively outcompeted their WT counterparts in the GC (competitive competency ∼1.6-fold; Figures 6H and 6I). Adoptively transferred *Foxo1*[M1L] mature B cells also successfully outcompeted WT B cells during GC responses to (4-Hydroxy-3-nitrophenylacetyl-Chicken Gamma Globulin) NP-CGG conjugate immunization in Ighel-MD4 hosts (∼2.2-fold; p < 0.01; Figures 6J–6L; STAR Methods)—indicating that this competitive advantage was due to B cell intrinsic effects.

Finally, we sought to determine whether such competitive advantage modified the course of disease in a lymphoma-prone background. *VavP-Bcl2* transgenic mice typically develop indolent malignancies resembling human follicular lymphoma (FL) (Egle et al., 2004); and acquisition of FOXO1 mutations in human FL correlates with histologic transformation into DLBCL (Bouska et al., 2017; Pasqualucci et al., 2014). We transduced bone marrow cells from *VavP-Bcl2* donor mice with retroviruses en-

coding for only GFP (EV) or WT or FOXO1 M1L plus GFP and used these cells to reconstitute hematopoiesis in lethally irradiated C57BL/6 mice, which were then repeatedly immunized upon engraftment and analyzed prior (∼100 days post-reconstitution; Figure S7A) to the onset of overt disease (∼300 days; Jiang et al., 2017; Teater et al., 2018). Compared to control C57BL/6 mice, all groups showed enlarged spleens and abnormal expansion of lymphoid compartments (Figures S7B and S7C) at expense of numerous (>3 per white pulp nodule), expansive centrocyte-rich PNA+ follicles with conserved follicular dendritic cell networks and Ki67+ B cells (Figure S7C, left panel). Minor differences in disease burden or histopathological features were found among groups (Figure S7C, right panel). Although the polyclonal nature of the lymphoid compartment (Figure S7D) was consistent with the histopathology and indicative of early-stage disease (Egle et al., 2004), we detected a significant increase in the fraction of FAS^{hi} B cells in the M1L group (Figures S7E and S7F), particularly FAS[hi]GL7^{lo} B cells—an abnormal B cell subset typically enriched in other Bcl2 cooperative models (Cai et al., 2020). The increased percentage of GFP+ cells within this population suggested that deregulated expression of FOXO1 favored the expansion of Bcl2+ B cells (∼69% versus 32%, p < 0.0001; Figures S7G and S7H). Most notably, FOXO1 M1L *VavP-Bcl2* B cells differed from FOXO1 WT and EV B cell pools in their signaling milieu, showing abnormal co-hyperactivation of PI3K (p-AKT) and SAPK/JNK (p-ATF2) signaling, as we had observed in human B cell lines (Figures S7I–S7K). Such signaling changes appeared to be favored during the expansion of precancerous B cells *in vivo*, along with subtle signs of disease acceleration.

In summary, the combination of *in vitro* and *in vivo* analyses in mouse models indicated that Foxo1 mutations confer B cells with effective functional and competitive advantages during immune activation in response to relevant GC signals, causing *in vivo* abnormal amplification of GC responses and favoring expansion of *Foxo1* mutant B cells with altered signaling (AKT and SAPK hyperactivation) during early stages of disease in a FL lymphoma model.

(B) Division index summaries (4–6 biological replicates per each group in A). Average ± SEM is shown (unpaired Student's t test).

(C) Representative flow cytometry analysis of cell proliferation in B cells stimulated for 72 h with lipopolysaccharides (LPS) (1 μg/mL) or RP105 (1 μg/mL). Division indices for each population are shown.

(D) Division index summaries (n = 6 LPS; n = 4 RP105). Average ± SEM is shown (unpaired Student's t test).

(E and F) Analysis of germinal center responses upon sheep red blood cell (SRBC) immunization (spleen, 12 days post-immunization).

(E) Representative contour plots, flow cytometry analysis of GC B cell fractions (B220+/GL7^{hi}/Fas[hi]).

(F) Results are summarized in graph; each symbol represents a single mouse. Mean ± SD is shown (unpaired Student's t test; see also Figures S6F–S6H).

(G–I) Analysis of competitive GC B cell expansion in mixed bone marrow chimeras.

(G) Schematic representation of experimental strategy. Irradiated host C57BL/6 mice were reconstituted with bone marrow progenitors isolated from *Foxo1*[WT/WT] or *Foxo1*[M1L/M1L] (CD45.2), mixed at 1:1 ratio with wild-type CD45.1/.2 progenitors, immunized, and analyzed 12 days later.

(H) Representative flow cytometry plots showing gating of GC B cells (B220+, FAS[hi], and GL7^{hi}) and non-GC B cells (B220+, Fas[lo], and Gl7^{lo}) in splenocytes from mixed chimeras.

(I) (Top panel) Representative flow cytometry histograms showing the distribution of CD45.1+ (CD45.1/2) and CD45.1− (CD45.2) B cells in GC and non-GC cell compartments. (Bottom panel) Competitive competencies for CD45.1− cells in GC B cell fractions are shown (see STAR Methods for details).
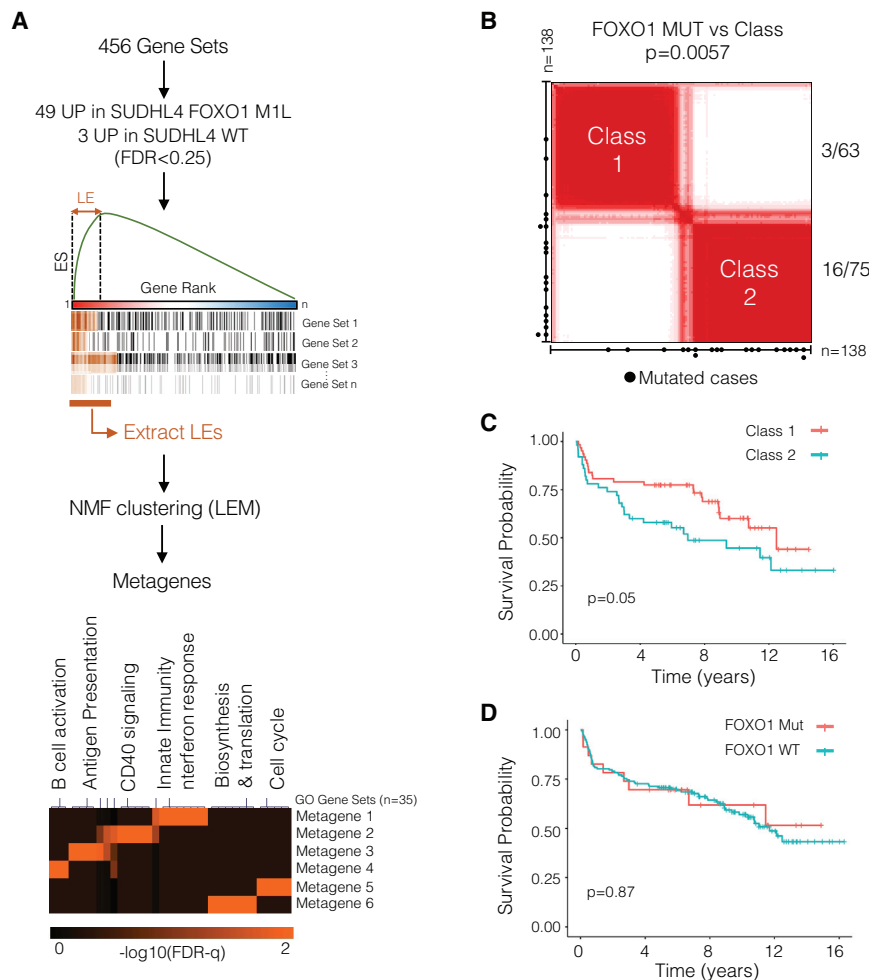
(J–L) Analysis of competitive GC B cell expansion upon B cell adoptive transfer in IghelMD4 mice.

(J) Schematic representation of experimental strategy (see STAR Methods for additional details).

(K) Gating strategy. GC B cells are gated as GL7^{hi}Fas[hi]. IghelMD4 B cells are IgD/Ma+ and respond poorly to (4-hydroxy-3-nitrophenyl)acetyl (NP)-peptide conjugates (Goodnow et al., 1988; Mason et al., 1992). Transferred in large numbers, donor B cells are preferentially recruited to GCs (compare IgD/Ma[hi] and IgD/Ma[lo] panels).

(L) (Top panel) Representative flow cytometry results, distribution of CD45.1+ (WT) and CD45.1− (*Foxo1*[WT/WT] or *Foxo1*[M1L/M1L]) B cells in IgD/Ma− GC and non-GC B cell fractions. (Bottom panel) Competitive competencies for CD45.1− donor cells are shown (n = 3 per group).

For all statistical tests, *p < 0.05; **p < 0.01; ***p < 0.001.

Figure 7. Functional FOXO1 mutant metagenes are conserved in human DLBCL and predict clinical outcome

(A) Definition of a functional classifier from RNA-seq data generated in WT versus mutant FOXO1 SUDHL4 isogenic clones. The leading edges of gene sets enriched at false discovery rate (FDR) < 0.25 in any group (WT versus mutant) were clustered into metagenes (Table S4; STAR Methods). Pathways significantly represented within these metagenes are shown as ssGSEA scores in the heatmap below.

(B) Consensus clustering of GCB-type DLBCL patient samples (n = 138) in two functional classes using ssGSEA scores for each metagene. The p value indicates the enrichment of mutant FOXO1 cases in class 1 versus class 2 (Fisher's exact test).

(C and D) Kaplan-Meier curves for survival probability (univariate analysis). DLBCL patients were stratified by functional class or mutational identity (n = 183). p values, log rank test.

Conservation of functional FOXO1 mutant gene signatures predicts clinical outcomes in diffuse large B cell lymphoma

Gene expression signatures can be used to identify patterns of pathway deregulation in tumors (e.g., B-NHLs) and inform classifications of conceptual, functional, clinical, and therapeutic significance (Aggarwal et al., 2009; Alizadeh et al., 2000; Bild et al., 2006; Huang et al., 2003; Victora et al., 2012). We thus reasoned that a "functional classifier" could better capture the aberrant activation of FOXO1 mutant gene signatures—reminiscent of GC B-cell-positive selection programs in primary DLBCL cases.

To generate this functional classifier (Figure 7A), we used a non-negative matrix factorization approach known as "leading edge metanalysis" (Godec et al., 2016; Reese et al., 2016; Tan et al., 2016), which helped us reduce 456 immune and B cell signaling gene sets into a small number of metagenes (n = 6), reflecting major biological themes linked to mutant FOXO1 activity. These metagenes were representative of key B cell programs, including CD40 signaling, immune activation, innate and interferon responses, and cell biosynthesis (Figure 7A; Table S4), typically initiated upon positive selection (Figure 5). We then estimated the activity of each of these metagenes in a set of primary DLBCL cases with available mutational, RNA-seq, and clinical

outcome data (Schmitz et al., 2018), centering our analysis on DLBCL cases of the GC B-cell-like type (n = 138)—closely related to the origin of SUDHL4 cells and enriched in N-terminal FOXO1 mutations. Clustering of DLBCL cases based on their metagene enrichment scores identified two "functional" classes (class 1: 63 cases; class 2: 75 cases; Figure 7B; Table S4; STAR Methods). A majority of DLBCL cases carrying FOXO1 mutations clustered together in one class (class 2, 16 versus 3; p = 5 × 10^{-3}; Fisher's exact test). Class 2 also included a sizeable number of cases without FOXO1 mutations, suggesting the possibility that other mutational makeups may support functional outcomes comparable to those driven by FOXO1 mutations (Figure 7B; Table S4). Similar results were obtained in a second series of DLBCL primary cases (n = 183; Arthur et al., 2018; Ennishi et al., 2019). These two functional classes associated with significant differences in clinical outcomes in an univariate analysis, with class 2 showing lower overall survival than class 1 (p = 0.05; median OS class 1: 12.47 years versus class 2: 6.96 years; Figure 7C). Unlike in previous reports (Trinh et al., 2013), FOXO1 mutations were not predictive of clinical outcomes unless associated to a functional signature (Figure 7D). We did not find any significant associations between these classes and DLBCL genetic subtypes (BN2/EZB/MCD/N1; Schmitz et al., 2018). Overall, these results show that the functional consequences of FOXO1 mutations, in the form of gene expression programs, can identify DLBCL functional groups with clinical predictive value.

DISCUSSION

Recent studies have suggested that the selection of missense mutations targeting FOXO1 in aggressive B-NHL reflect the

need for tumoral cells to maintain considerable amounts of nuclear FOXO1 and escape PI3K inhibition. The apparent dependency of tumoral cells on mutant FOXO1 for their growth and survival suggested the notion that "hyperactive" FOXO1 variants are required to support lymphomagenesis (Kabrani et al., 2018; Trinh et al., 2013; Zhou et al., 2019). Rather, we demonstrate that these mutations create partially hypomorphic FOXO1 protein variants with altered transcriptional repertoires and biological activities, driving phenotypes analogous to positively selected GC B cells. These findings reconcile conflicting observations and provide new insights into the contributions of FOXO1 to the control of GC responses and lymphomagenesis.

A large fraction (~50%) of FOXO1 missense mutations in B-NHL encode amino acid residues surrounding T24 (R19-L27), a known AKT phosphorylation site (Calnan and Brunet, 2008). These mutations abrogate or severely impair T24 phosphorylation. The R19-L27 region is also lost (truncation) in M1L FOXO1 mutant proteins. The current notion is that all these mutant proteins would escape negative regulation by PI3K/AKT (Kabrani et al., 2018; Trinh et al., 2013), which promotes FOXO1 nuclear export and inactivation (Calnan and Brunet, 2008). Indeed, loss of T24 phosphorylation in engineered B cells results in FOXO1 nuclear accumulation (Kabrani et al., 2018). However, this concept is disputed by the lack of significant correlation between the subcellular distribution of FOXO1 protein and PI3K pathway activity in our analysis of primary DLBCL cases and equivalent findings in BL (Zhou et al., 2019). In fact, we find that FOXO1 mutant proteins do respond to PI3K signaling.

These discordant observations may underlie transcription and signaling effects of mutant FOXO1 proteins (Eijkelenboom and Burgering, 2013; Puig and Tjian, 2005). The concurrent hyperactivation of both AKT and SAPK/JNK kinases in FOXO1 mutant B cells disrupts the usual counterbalance between these two pathways, particularly relevant under low PI3K/AKT signals (SAPK/JNK would be dominant) or when FOXO1 phosphorylation by AKT is splintered by cancer mutations, and effectively contributes to the nuclear retention of FOXO1 mutant proteins. Specific processes where balance between PI3K and SAPK/JNK signaling determines cell fate, such as starvation, immune activation, and cancer progression (Hübner et al., 2012; Vivanco et al., 2007), may be particularly permissive to the expansion of FOXO1 mutant B cells. Consistently, we find that abnormal co-activation of AKT and JNK/ATF2 is favored during early malignant transformation in combined *VavP-Bcl2/Foxo1^{M1L}* chimeras.

One notable finding is that FOXO1 mutant proteins behave as partial hypomorphs, exemplified by the reduced affinity for specific target genes, differences in DNA motif selection, and altered transcriptional repertoires. These changes result in activation of immune gene programs directly regulated by Foxo1 in mouse GC B cells and abnormally hyperactivated in *Foxo1*-null GCs (Dominguez-Sola et al., 2015; Inoue et al., 2017; Sander et al., 2015); and these effects are dominant—independent of allele dosage. Post-translational modifications and, notably, T24 mutations can likely impact FOXO1 affinity and/or transcriptional outputs at target genes (Brent et al., 2008; Langlet et al., 2017; Matsuzaki et al., 2005), particularly the ability to repress transcription (Nakae et al., 2000).

Overall, the complex phenotype of FOXO1 mutant B cells is strongly reminiscent of positive selection. FOXO1 effectively captures and integrates signals from CD40 and BCR, relayed by PI3K/AKT and SAPK/JNK via phosphorylation, to initiate key immune gene expression programs. Our observations suggest that FOXO1 is a hub for signals leading to positive selection and that dysregulation of this activity upon mutation may facilitate the aberrant selection, survival, and expansion of B cells in absence of strong, synergistic signals. Such properties would endow FOXO1 mutant B cells with a significant competitive advantage during GC responses, as we demonstrate in mixed chimeras and adoptive transfer experiments.

A substantial fraction of genomic abnormalities in GC-derived B-NHL are predicted to impact pathways and processes essential to GC biology (Basso and Dalla-Favera, 2015; Mlynarczyk et al., 2019). We used functional "metagenes" (Godec et al., 2016; Reese et al., 2016) to find indication of FOXO1 mutant transcriptional activities in primary DLBCL cases, with strong correlations with FOXO1 mutational status and clinical outcome. These same "mutant" programs were also identified in a sizeable number of FOXO1 unmutated cases, indicating that other genomic abnormalities may alter biological processes controlled by FOXO1 in GC B cells. Thus, equivalent functional outcomes—specifically, the activation of programs resembling positive selection—may have been selected during lymphoma pathogenesis through alternate mutational histories, a notion amenable to future investigation. The bypass of affinity-selection checkpoints may represent a major pathogenic mechanism in GC-derived B-NHLs: using this strategy, mutant GC B cells would gain critical competitive advantage for their selective expansion during early lymphomagenesis.

Limitations of the study

The underlying mechanism by which mutations centered around the T24 site alter FOXO1 DNA binding affinities was not examined; neither did we explore whether mutations targeting the DNA binding domain may co-opt similar mechanisms to cause equivalent phenotypes to those described here. Dedicated models and molecular and structural studies will be required to solve these questions. We also note that, although our experiments imply that FOXO1 mutant phenotypes are B cell intrinsic, we cannot rule out that some of the effects also require T cell help (e.g., altered dark-to-light zone ratios, which were not examined in the cell transfer experiments). Moreover, unnoticed defects during B cell development (for example, during the establishment of central tolerance) could also underlie some of these phenotypes. Access to conditional models, as opposed to the constitutive model reported here, would help address these points and facilitate more comprehensive follow-up studies, particularly on the role of FOXO1 mutations during lymphomagenesis. Such studies could also help refine the functional signature defined in this manuscript, perhaps by including potential correlations with the analysis of SAPK/JNK signaling in primary DLBCL cases. Although useful to conceptualize disease pathogenesis and stratify patients, this functional signature only associated with clinical outcome in univariate analysis —in multivariate analyses, outcome effects are heavily influenced by International Prognostic Index (IPI) and DHIT (double-hit) scores, noting that high IPI or DHIT cases are more common in class 2 (data not shown).

STAR★METHODS

Detailed methods are provided in the online version of this paper and include the following:

SUPPORTING CITATIONS

The following references appear in the Supplemental information: Chen et al. (2010); Fuchs et al. (2000); Pasqualucci et al. (2001); Petro et al. (2002); Su and Rawlings (2002); Teague et al. (2007).

REFERENCES

Aggarwal, M., Sánchez-Beato, M., Gómez-López, G., Al-Shahrour, F., Martínez, N., Rodríguez, A., Ruiz-Ballesteros, E., Camacho, F.I., Pérez-Rosado, A., de la Cueva, P., et al. (2009). Functional signatures identified in B-cell non-Hodgkin lymphoma profiles. Leuk. Lymphoma *50*, 1699–1708.

Alizadeh, A.A., Eisen, M.B., Davis, R.E., Ma, C., Lossos, I.S., Rosenwald, A., Boldrick, J.C., Sabet, H., Tran, T., Yu, X., et al. (2000). Distinct types of diffuse

large B-cell lymphoma identified by gene expression profiling. Nature 403, 503–511.

Anders, S., Pyl, P.T., and Huber, W. (2015). HTSeq–a Python framework to work with high-throughput sequencing data. Bioinformatics 31, 166–169.

Arthur, S.E., Jiang, A., Grande, B.M., Alcaide, M., Cojocaru, R., Rushton, C.K., Mottok, A., Hilton, L.K., Lat, P.K., Zhao, E.Y., et al. (2018). Genome-wide discovery of somatic regulatory variants in diffuse large B-cell lymphoma. Nat. Commun. 9, 4001.

Baffi, T.R., Cohen-Katsenelson, K., and Newton, A.C. (2021). PHLPPing the script: emerging roles of PHLPP phosphatases in cell signaling. Annu. Rev. Pharmacol. Toxicol. 61, 723–743.

Bankhead, P., Loughrey, M.B., Fernández, J.A., Dombrowski, Y., McArt, D.G., Dunne, P.D., McQuaid, S., Gray, R.T., Murray, L.J., Coleman, H.G., et al. (2017). QuPath: open source software for digital pathology image analysis. Sci. Rep. 7, 16878.

Barbie, D.A., Tamayo, P., Boehm, J.S., Kim, S.Y., Moody, S.E., Dunn, I.F., Schinzel, A.C., Sandy, P., Meylan, E., Scholl, C., et al. (2009). Systematic RNA interference reveals that oncogenic KRAS-driven cancers require TBK1. Nature 462, 108–112.

Basso, K., and Dalla-Favera, R. (2015). Germinal centres and B cell lymphomagenesis. Nat. Rev. Immunol. 15, 172–184.

Basso, K., Klein, U., Niu, H., Stolovitzky, G.A., Tu, Y., Califano, A., Cattoretti, G., and Dalla-Favera, R. (2004). Tracking CD40 signaling during germinal center development. Blood 104, 4088–4096.

Basu, S., Ray, A., and Dittel, B.N. (2013). Differential representation of B cell subsets in mixed bone marrow chimera mice due to expression of allelic variants of CD45 (CD45.1/CD45.2). J. Immunol. Methods 396, 163–167.

Berberich, I., Shu, G., Siebelt, F., Woodgett, J.R., Kyriakis, J.M., and Clark, E.A. (1996). Cross-linking CD40 on B cells preferentially induces stress-activated protein kinases rather than mitogen-activated protein kinases. EMBO J. 15, 92–101.

Bild, A.H., Yao, G., Chang, J.T., Wang, Q., Potti, A., Chasse, D., Joshi, M.B., Harpole, D., Lancaster, J.M., Berchuck, A., et al. (2006). Oncogenic pathway signatures in human cancers as a guide to targeted therapies. Nature 439, 353–357.

Bouska, A., Zhang, W., Gong, Q., Iqbal, J., Scuto, A., Vose, J., Ludvigsen, M., Fu, K., Weisenburger, D.D., Greiner, T.C., et al. (2017). Combined copy number and mutation analysis identifies oncogenic pathways associated with transformation of follicular lymphoma. Leukemia 31, 83–91.

Brent, M.M., Anand, R., and Marmorstein, R. (2008). Structural basis for DNA recognition by FoxO1 and its regulation by posttranslational modification. Structure 16, 1407–1416.

Brognard, J., Sierecki, E., Gao, T., and Newton, A.C. (2007). PHLPP and a second isoform, PHLPP2, differentially attenuate the amplitude of Akt signaling by regulating distinct Akt isoforms. Mol. Cell 25, 917–931.

Cai, Z., Zhang, L., Cao, M., Wang, Y., Wang, F., Bian, W., Zhai, S., and Wang, X. (2020). Generation of a murine model for c-MYC and BCL2 co-expression B cell lymphomas. Front. Oncol. 10, 1007.

Calado, D.P., Sasaki, Y., Godinho, S.A., Pellerin, A., Köchert, K., Sleckman, B.P., de Alborán, I.M., Janz, M., Rodig, S., and Rajewsky, K. (2012). The cell-cycle regulator c-Myc is essential for the formation and maintenance of germinal centers. Nat. Immunol. 13, 1092–1100.

Calnan, D.R., and Brunet, A. (2008). The FoxO code. Oncogene 27, 2276–2288.

Chaplin, J.W., Kasahara, S., Clark, E.A., and Ledbetter, J.A. (2011). Anti-CD180 (RP105) activates B cells to rapidly produce polyclonal Ig via a T cell and MyD88-independent pathway. J. Immunol. 187, 4199–4209.

Chaveroux, C., Jousse, C., Cherasse, Y., Maurin, A.C., Parry, L., Carraro, V., Derijard, B., Bruhat, A., and Fafournoux, P. (2009). Identification of a novel amino acid response pathway triggering ATF2 phosphorylation in mammals. Mol. Cell. Biol. 29, 6515–6526.

Chen, J., Limon, J.J., Blanc, C., Peng, S.L., and Fruman, D.A. (2010). Foxo1 regulates marginal zone B-cell development. Eur. J. Immunol. 40, 1890–1896.

Chen, M., Pratt, C.P., Zeeman, M.E., Schultz, N., Taylor, B.S., O'Neill, A., Castillo-Martin, M., Nowak, D.G., Naguib, A., Grace, D.M., et al. (2011). Identification of PHLPP1 as a tumor suppressor reveals the role of feedback activation in PTEN-mutant prostate cancer progression. Cancer Cell 20, 173–186.

Compagno, M., Wang, Q., Pighi, C., Cheong, T.C., Meng, F.L., Poggio, T., Yeap, L.S., Karaca, E., Blasco, R.B., Langellotto, F., et al. (2017). Phosphatidylinositol 3-kinase δ blockade increases genomic instability in B cells. Nature 542, 489–493.

Cong, L., Ran, F.A., Cox, D., Lin, S., Barretto, R., Habib, N., Hsu, P.D., Wu, X., Jiang, W., Marraffini, L.A., and Zhang, F. (2013). Multiplex genome engineering using CRISPR/Cas systems. Science 339, 819–823.

Dengler, H.S., Baracho, G.V., Omori, S.A., Bruckner, S., Arden, K.C., Castrillon, D.H., DePinho, R.A., and Rickert, R.C. (2008). Distinct functions for the transcription factor Foxo1 at various stages of B cell differentiation. Nat. Immunol. 9, 1388–1398.

Dominguez-Sola, D., and Cattoretti, G. (2017). Analysis of the germinal center reaction in tissue sections. Methods Mol. Biol. 1623, 1–20.

Dominguez-Sola, D., Victora, G.D., Ying, C.Y., Phan, R.T., Saito, M., Nussenzweig, M.C., and Dalla-Favera, R. (2012). The proto-oncogene MYC is required for selection in the germinal center and cyclic reentry. Nat. Immunol. 13, 1083–1091.

Dominguez-Sola, D., Kung, J., Holmes, A.B., Wells, V.A., Mo, T., Basso, K., and Dalla-Favera, R. (2015). The FOXO1 transcription factor instructs the germinal center dark zone program. Immunity 43, 1064–1074.

Egle, A., Harris, A.W., Bath, M.L., O'Reilly, L., and Cory, S. (2004). VavP-Bcl2 transgenic mice develop follicular lymphoma preceded by germinal center hyperplasia. Blood 103, 2276–2283.

Eijkelenboom, A., and Burgering, B.M. (2013). FOXOs: signalling integrators for homeostasis maintenance. Nat. Rev. Mol. Cell Biol. 14, 83–97.

Ennishi, D., Jiang, A., Boyle, M., Collinge, B., Grande, B.M., Ben-Neriah, S., Rushton, C., Tang, J., Thomas, N., Slack, G.W., et al. (2019). Double-hit gene expression signature defines a distinct subgroup of germinal center B-cell-like diffuse large B-cell lymphoma. J. Clin. Oncol. 37, 190–201.

Ersching, J., Efeyan, A., Mesin, L., Jacobsen, J.T., Pasqual, G., Grabiner, B.C., Dominguez-Sola, D., Sabatini, D.M., and Victora, G.D. (2017). Germinal center selection and affinity maturation require dynamic regulation of mTORC1 kinase. Immunity 46, 1045–1058.e6.

Essers, M.A., Weijzen, S., de Vries-Smits, A.M., Saarloos, I., de Ruiter, N.D., Bos, J.L., and Burgering, B.M. (2004). FOXO transcription factor activation by oxidative stress mediated by the small GTPase Ral and JNK. EMBO J. 23, 4802–4812.

Fellmann, C., Hoffmann, T., Sridhar, V., Hopfgartner, B., Muhar, M., Roth, M., Lai, D.Y., Barbosa, I.A., Kwon, J.S., Guan, Y., et al. (2013). An optimized microRNA backbone for effective single-copy RNAi. Cell Rep. 5, 1704–1713.

Fruman, D.A., Chiu, H., Hopkins, B.D., Bagrodia, S., Cantley, L.C., and Abraham, R.T. (2017). The PI3K pathway in human disease. Cell 170, 605–635.

Fuchs, S.Y., Tappin, I., and Ronai, Z. (2000). Stability of the ATF2 transcription factor is regulated by phosphorylation and dephosphorylation. J. Biol. Chem. 275, 12560–12564.

Fulda, S., Gorman, A.M., Hori, O., and Samali, A. (2010). Cellular stress responses: cell survival and cell death. Int. J. Cell Biol. 2010, 214074.

Furuyama, T., Nakazawa, T., Nakano, I., and Mori, N. (2000). Identification of the differential distribution patterns of mRNAs and consensus binding sequences for mouse DAF-16 homologues. Biochem. J. 349, 629–634.

Gallagher, E., Enzler, T., Matsuzawa, A., Anzelon-Mills, A., Otero, D., Holzer, R., Janssen, E., Gao, M., and Karin, M. (2007). Kinase MEKK1 is required for CD40-dependent activation of the kinases Jnk and p38, germinal center formation, B cell proliferation and antibody production. Nat. Immunol. 8, 57–63.

Gao, T., Furnari, F., and Newton, A.C. (2005). PHLPP: a phosphatase that directly dephosphorylates Akt, promotes apoptosis, and suppresses tumor growth. Mol. Cell 18, 13–24.

Godec, J., Tan, Y., Liberzon, A., Tamayo, P., Bhattacharya, S., Butte, A.J., Mesirov, J.P., and Haining, W.N. (2016). Compendium of immune signatures

identifies conserved and species-specific biology in response to inflammation. Immunity *44*, 194–206.

Goodnow, C.C., Crosbie, J., Adelstein, S., Lavoie, T.B., Smith-Gill, S.J., Brink, R.A., Pritchard-Briscoe, H., Wotherspoon, J.S., Loblay, R.H., Raphael, K., et al. (1988). Altered immunoglobulin expression and functional silencing of self-reactive B lymphocytes in transgenic mice. Nature *334*, 676–682.

Grande, B.M., Gerhard, D.S., Jiang, A., Griner, N.B., Abramson, J.S., Alexander, T.B., Allen, H., Ayers, L.W., Bethony, J.M., Bhatia, K., et al. (2019). Genome-wide discovery of somatic coding and noncoding mutations in pediatric endemic and sporadic Burkitt lymphoma. Blood *133*, 1313–1324.

Heinz, S., Benner, C., Spann, N., Bertolino, E., Lin, Y.C., Laslo, P., Cheng, J.X., Murre, C., Singh, H., and Glass, C.K. (2010). Simple combinations of lineage-determining transcription factors prime cis-regulatory elements required for macrophage and B cell identities. Mol. Cell *38*, 576–589.

Hotamisligil, G.S., and Davis, R.J. (2016). Cell signaling and stress responses. Cold Spring Harb. Perspect. Biol. *8*, a006072.

Huang, C.Y., Bredemeyer, A.L., Walker, L.M., Bassing, C.H., and Sleckman, B.P. (2008). Dynamic regulation of c-Myc proto-oncogene expression during lymphocyte development revealed by a GFP-c-Myc knock-in mouse. Eur. J. Immunol. *38*, 342–349.

Huang, E., Ishida, S., Pittman, J., Dressman, H., Bild, A., Kloos, M., D'Amico, M., Pestell, R.G., West, M., and Nevins, J.R. (2003). Gene expression phenotypic models that predict the activity of oncogenic pathways. Nat. Genet. *34*, 226–230.

Huang, H., and Tindall, D.J. (2007). Dynamic FoxO transcription factors. J. Cell Sci. *120*, 2479–2487.

Hübner, A., Mulholland, D.J., Standen, C.L., Karasarides, M., Cavanagh-Kyros, J., Barrett, T., Chi, H., Greiner, D.L., Tournier, C., Sawyers, C.L., et al. (2012). JNK and PTEN cooperatively control the development of invasive adenocarcinoma of the prostate. Proc. Natl. Acad. Sci. USA *109*, 12046–12051.

Inoue, T., Shinnakasu, R., Ise, W., Kawai, C., Egawa, T., and Kurosaki, T. (2017). The transcription factor Foxo1 controls germinal center B cell proliferation in response to T cell help. J. Exp. Med. *214*, 1181–1198.

Jiang, Y., Ortega-Molina, A., Geng, H., Ying, H.Y., Hatzi, K., Parsa, S., McNally, D., Wang, L., Doane, A.S., Agirre, X., et al. (2017). CREBBP inactivation promotes the development of HDAC3-dependent lymphomas. Cancer Discov. *7*, 38–53.

Kabrani, E., Chu, V.T., Tasouri, E., Sommermann, T., Baßler, K., Ulas, T., Zenz, T., Bullinger, L., Schultze, J.L., Rajewsky, K., and Sander, S. (2018). Nuclear FOXO1 promotes lymphomagenesis in germinal center B cells. Blood *132*, 2670–2683.

Langlet, F., Haeusler, R.A., Lindén, D., Ericson, E., Norris, T., Johansson, A., Cook, J.R., Aizawa, K., Wang, L., Buettner, C., and Accili, D. (2017). Selective inhibition of FOXO1 activator/repressor balance modulates hepatic glucose handling. Cell *171*, 824–835.e18.

Langmead, B., and Salzberg, S.L. (2012). Fast gapped-read alignment with Bowtie 2. Nat. Methods *9*, 357–359.

Law, C.W., Chen, Y., Shi, W., and Smyth, G.K. (2014). voom: precision weights unlock linear model analysis tools for RNA-seq read counts. Genome Biol. *15*, R29.

Li, H., Handsaker, B., Wysoker, A., Fennell, T., Ruan, J., Homer, N., Marth, G., Abecasis, G., and Durbin, R.; 1000 Genome Project Data Processing Subgroup (2009). The Sequence Alignment/Map format and SAMtools. Bioinformatics *25*, 2078–2079.

Li, Y.Y., Baccam, M., Waters, S.B., Pessin, J.E., Bishop, G.A., and Koretzky, G.A. (1996). CD40 ligation results in protein kinase C-independent activation of ERK and JNK in resting murine splenic B cells. J. Immunol. *157*, 1440–1447.

Liao, Y., Smyth, G.K., and Shi, W. (2014). featureCounts: an efficient general purpose program for assigning sequence reads to genomic features. Bioinformatics *30*, 923–930.

Lin, Y.C., Jhunjhunwala, S., Benner, C., Heinz, S., Welinder, E., Mansson, R., Sigvardsson, M., Hagman, J., Espinoza, C.A., Dutkowski, J., et al. (2010). A global network of transcription factors, involving E2A, EBF1 and Foxo1, that orchestrates B cell fate. Nat. Immunol. *11*, 635–643.

Love, M.I., Huber, W., and Anders, S. (2014). Moderated estimation of fold change and dispersion for RNA-seq data with DESeq2. Genome Biol. *15*, 550.

Lu, P., Shih, C., and Qi, H. (2017). Ephrin B1-mediated repulsion and signaling control germinal center T cell territoriality and function. Science *356*, eaai9264.

Luo, W., Weisel, F., and Shlomchik, M.J. (2018). B cell receptor and CD40 signaling are rewired for synergistic induction of the c-Myc transcription factor in germinal center B cells. Immunity *48*, 313–326.e5.

Mason, D.Y., Jones, M., and Goodnow, C.C. (1992). Development and follicular localization of tolerant B lymphocytes in lysozyme/anti-lysozyme IgM/IgD transgenic mice. Int. Immunol. *4*, 163–175.

Matheson, N.J., Peden, A.A., and Lehner, P.J. (2014). Antibody-free magnetic cell sorting of genetically modified primary human CD4+ T cells by one-step streptavidin affinity purification. PLoS ONE *9*, e111437.

Matsuzaki, H., Daitoku, H., Hatta, M., Aoyama, H., Yoshimochi, K., and Fukamizu, A. (2005). Acetylation of Foxo1 alters its DNA-binding ability and sensitivity to phosphorylation. Proc. Natl. Acad. Sci. USA *102*, 11278–11283.

Mesin, L., Ersching, J., and Victora, G.D. (2016). Germinal center B cell dynamics. Immunity *45*, 471–482.

Mlynarczyk, C., Fontán, L., and Melnick, A. (2019). Germinal center-derived lymphomas: the darkest side of humoral immunity. Immunol. Rev. *288*, 214–239.

Monti, S., Tamayo, P., Mesirov, J., and Golub, T. (2003). Consensus clustering: a resampling-based method for class discovery and visualization of gene expression microarray data. Mach. Learn. *52*, 91–118.

Morin, R.D., Assouline, S., Alcaide, M., Mohajeri, A., Johnston, R.L., Chong, L., Grewal, J., Yu, S., Fornika, D., Bushell, K., et al. (2016). Genetic landscapes of relapsed and refractory diffuse large B-cell lymphomas. Clin. Cancer Res. *22*, 2290–2300.

Morin, R.D., Mungall, K., Pleasance, E., Mungall, A.J., Goya, R., Huff, R.D., Scott, D.W., Ding, J., Roth, A., Chiu, R., et al. (2013). Mutational and structural analysis of diffuse large B-cell lymphoma using whole-genome sequencing. Blood *122*, 1256–1265.

Nakae, J., Barr, V., and Accili, D. (2000). Differential regulation of gene expression by insulin and IGF-1 receptors correlates with phosphorylation of a single amino acid residue in the forkhead transcription factor FKHR. EMBO J. *19*, 989–996.

Obsil, T., and Obsilova, V. (2011). Structural basis for DNA recognition by FOXO proteins. Biochim. Biophys. Acta *1813*, 1946–1953.

Ogata, H., Su, I., Miyake, K., Nagai, Y., Akashi, S., Mecklenbräuker, I., Rajewsky, K., Kimoto, M., and Tarakhovsky, A. (2000). The toll-like receptor protein RP105 regulates lipopolysaccharide signaling in B cells. J. Exp. Med. *192*, 23–29.

Paik, J.H., Kollipara, R., Chu, G., Ji, H., Xiao, Y., Ding, Z., Miao, L., Tothova, Z., Horner, J.W., Carrasco, D.R., et al. (2007). FoxOs are lineage-restricted redundant tumor suppressors and regulate endothelial cell homeostasis. Cell *128*, 309–323.

Pasqualucci, L., Neumeister, P., Goossens, T., Nanjangud, G., Chaganti, R.S., Küppers, R., and Dalla-Favera, R. (2001). Hypermutation of multiple proto-oncogenes in B-cell diffuse large-cell lymphomas. Nature *412*, 341–346.

Pasqualucci, L., Khiabanian, H., Fangazio, M., Vasishtha, M., Messina, M., Holmes, A.B., Ouillette, P., Trifonov, V., Rossi, D., Tabbò, F., et al. (2014). Genetics of follicular lymphoma transformation. Cell Rep. *6*, 130–140.

Pelossof, R., Fairchild, L., Huang, C.H., Widmer, C., Sreedharan, V.T., Sinha, N., Lai, D.Y., Guan, Y., Premsrirut, P.K., Tschaharganeh, D.F., et al. (2017). Prediction of potent shRNAs with a sequential classification algorithm. Nat. Biotechnol. *35*, 350–353.

Petro, J.B., Gerstein, R.M., Lowe, J., Carter, R.S., Shinners, N., and Khan, W.N. (2002). Transitional type 1 and 2 B lymphocyte subsets are differentially responsive to antigen receptor signaling. J. Biol. Chem. *277*, 48009–48019.

Puig, O., and Tjian, R. (2005). Transcriptional feedback control of insulin receptor by dFOXO/FOXO1. Genes Dev. *19*, 2435–2446.

Ramírez, F., Ryan, D.P., Grüning, B., Bhardwaj, V., Kilpert, F., Richter, A.S., Heyne, S., Dündar, F., and Manke, T. (2016). deepTools2: a next generation web server for deep-sequencing data analysis. Nucleic Acids Res. 44 (W1), W160–W165.

Ran, F.A., Hsu, P.D., Wright, J., Agarwala, V., Scott, D.A., and Zhang, F. (2013). Genome engineering using the CRISPR-Cas9 system. Nat. Protoc. 8, 2281–2308.

Reese, T.A., Bi, K., Kambal, A., Filali-Mouhim, A., Beura, L.K., Bürger, M.C., Pulendran, B., Sekaly, R.P., Jameson, S.C., Masopust, D., et al. (2016). Sequential infection with common pathogens promotes human-like immune gene expression and altered vaccine response. Cell Host Microbe 19, 713–719.

Reich, M., Liefeld, T., Gould, J., Lerner, J., Tamayo, P., and Mesirov, J.P. (2006). GenePattern 2.0. Nat. Genet. 38, 500–501.

Richter, K.N., Revelo, N.H., Seitz, K.J., Helm, M.S., Sarkar, D., Saleeb, R.S., D'Este, E., Eberle, J., Wagner, E., Vogl, C., et al. (2018). Glyoxal as an alternative fixative to formaldehyde in immunostaining and super-resolution microscopy. EMBO J. 37, 139–159.

Rickert, R.C. (2013). New insights into pre-BCR and BCR signalling with relevance to B cell malignancies. Nat. Rev. Immunol. 13, 578–591.

Rueden, C.T., Schindelin, J., Hiner, M.C., DeZonia, B.E., Walter, A.E., Arena, E.T., and Eliceiri, K.W. (2017). ImageJ2: ImageJ for the next generation of scientific image data. BMC Bioinformatics 18, 529.

Sakata, N., Patel, H.R., Terada, N., Aruffo, A., Johnson, G.L., and Gelfand, E.W. (1995). Selective activation of c-Jun kinase mitogen-activated protein kinase by CD40 on human B cells. J. Biol. Chem. 270, 30823–30828.

Sander, S., Chu, V.T., Yasuda, T., Franklin, A., Graf, R., Calado, D.P., Li, S., Imami, K., Selbach, M., Di Virgilio, M., et al. (2015). PI3 kinase and FOXO1 transcription factor activity differentially control B cells in the germinal center light and dark zones. Immunity 43, 1075–1086.

Schmitz, R., Wright, G.W., Huang, D.W., Johnson, C.A., Phelan, J.D., Wang, J.Q., Roulland, S., Kasbekar, M., Young, R.M., Shaffer, A.L., et al. (2018). Genetics and pathogenesis of diffuse large B-cell lymphoma. N. Engl. J. Med. 378, 1396–1407.

Shaffer, A.L., 3rd, Young, R.M., and Staudt, L.M. (2012). Pathogenesis of human B cell lymphomas. Annu. Rev. Immunol. 30, 565–610.

Srinivasan, L., Sasaki, Y., Calado, D.P., Zhang, B., Paik, J.H., DePinho, R.A., Kutok, J.L., Kearney, J.F., Otipoby, K.L., and Rajewsky, K. (2009). PI3 kinase signals BCR-dependent mature B cell survival. Cell 139, 573–586.

Su, T.T., and Rawlings, D.J. (2002). Transitional B lymphocyte subsets operate as distinct checkpoints in murine splenic B cell development. J. Immunol. 168, 2101–2110.

Su, Y.W., Hao, Z., Hirao, A., Yamamoto, K., Lin, W.J., Young, A., Duncan, G.S., Yoshida, H., Wakeham, A., Lang, P.A., et al. (2011). 14-3-3sigma regulates B-cell homeostasis through stabilization of FOXO1. Proc. Natl. Acad. Sci. USA 108, 1555–1560.

Subramanian, A., Tamayo, P., Mootha, V.K., Mukherjee, S., Ebert, B.L., Gillette, M.A., Paulovich, A., Pomeroy, S.L., Golub, T.R., Lander, E.S., and Mesirov, J.P. (2005). Gene set enrichment analysis: a knowledge-based approach for interpreting genome-wide expression profiles. Proc. Natl. Acad. Sci. USA 102, 15545–15550.

Szczepankiewicz, B.G., Kosogof, C., Nelson, L.T., Liu, G., Liu, B., Zhao, H., Serby, M.D., Xin, Z., Liu, M., Gum, R.J., et al. (2006). Aminopyridine-based c-Jun N-terminal kinase inhibitors with cellular activity and minimal cross-kinase activity. J. Med. Chem. 49, 3563–3580.

Tan, Y.G.J., Wu, F., Tamayo, P., Mesirov, J.P., and Haining, W.N. (2016). A method for downstream analysis of gene set enrichment results facilitates the biological interpretation of vaccine efficacy studies. bioRxiv.

Teague, B.N., Pan, Y., Mudd, P.A., Nakken, B., Zhang, Q., Szodoray, P., Kim-Howard, X., Wilson, P.C., and Farris, A.D. (2007). Cutting edge: transitional T3 B cells do not give rise to mature B cells, have undergone selection, and are reduced in murine lupus. J. Immunol. 178, 7511–7515.

Teater, M., Dominguez, P.M., Redmond, D., Chen, Z., Ennishi, D., Scott, D.W., Cimmino, L., Ghione, P., Chaudhuri, J., Gascoyne, R.D., et al. (2018). AICDA drives epigenetic heterogeneity and accelerates germinal center-derived lymphomagenesis. Nat. Commun. 9, 222.

Trapnell, C., Pachter, L., and Salzberg, S.L. (2009). TopHat: discovering splice junctions with RNA-Seq. Bioinformatics 25, 1105–1111.

Trapnell, C., Williams, B.A., Pertea, G., Mortazavi, A., Kwan, G., van Baren, M.J., Salzberg, S.L., Wold, B.J., and Pachter, L. (2010). Transcript assembly and quantification by RNA-Seq reveals unannotated transcripts and isoform switching during cell differentiation. Nat. Biotechnol. 28, 511–515.

Trinh, D.L., Scott, D.W., Morin, R.D., Mendez-Lago, M., An, J., Jones, S.J., Mungall, A.J., Zhao, Y., Schein, J., Steidl, C., et al. (2013). Analysis of FOXO1 mutations in diffuse large B-cell lymphoma. Blood 121, 3666–3674.

Tsai, K.L., Sun, Y.J., Huang, C.Y., Yang, J.Y., Hung, M.C., and Hsiao, C.D. (2007). Crystal structure of the human FOXO3a-DBD/DNA complex suggests the effects of post-translational modification. Nucleic Acids Res. 35, 6984–6994.

Van Der Heide, L.P., Hoekman, M.F., and Smidt, M.P. (2004). The ins and outs of FoxO shuttling: mechanisms of FoxO translocation and transcriptional regulation. Biochem. J. 380, 297–309.

Victora, G.D., Dominguez-Sola, D., Holmes, A.B., Deroubaix, S., Dalla-Favera, R., and Nussenzweig, M.C. (2012). Identification of human germinal center light and dark zone cells and their relationship to human B-cell lymphomas. Blood 120, 2240–2248.

Victora, G.D., and Mesin, L. (2014). Clonal and cellular dynamics in germinal centers. Curr. Opin. Immunol. 28, 90–96.

Victora, G.D., and Nussenzweig, M.C. (2012). Germinal centers. Annu. Rev. Immunol. 30, 429–457.

Victora, G.D., Schwickert, T.A., Fooksman, D.R., Kamphorst, A.O., Meyer-Hermann, M., Dustin, M.L., and Nussenzweig, M.C. (2010). Germinal center dynamics revealed by multiphoton microscopy with a photoactivatable fluorescent reporter. Cell 143, 592–605.

Vivanco, I., Palaskas, N., Tran, C., Finn, S.P., Getz, G., Kennedy, N.J., Jiao, J., Rose, J., Xie, W., Loda, M., et al. (2007). Identification of the JNK signaling pathway as a functional target of the tumor suppressor PTEN. Cancer Cell 11, 555–569.

Wang, M.C., Bohmann, D., and Jasper, H. (2005). JNK extends life span and limits growth by antagonizing cellular and organism-wide responses to insulin signaling. Cell 121, 115–125.

Xie, L., Ushmorov, A., Leithäuser, F., Guan, H., Steidl, C., Färbinger, J., Pelzer, C., Vogel, M.J., Maier, H.J., Gascoyne, R.D., et al. (2012). FOXO1 is a tumor suppressor in classical Hodgkin lymphoma. Blood 119, 3503–3511.

Yusuf, I., Zhu, X., Kharas, M.G., Chen, J., and Fruman, D.A. (2004). Optimal B-cell proliferation requires phosphoinositide 3-kinase-dependent inactivation of FOXO transcription factors. Blood 104, 784–787.

Zanella, F., Rosado, A., Garcia, B., Carnero, A., and Link, W. (2009). Using multiplexed regulation of luciferase activity and GFP translocation to screen for FOXO modulators. BMC Cell Biol. 10, 14.

Zhang, Y., Liu, T., Meyer, C.A., Eeckhoute, J., Johnson, D.S., Bernstein, B.E., Nusbaum, C., Myers, R.M., Brown, M., Li, W., and Liu, X.S. (2008). Model-based analysis of ChIP-seq (MACS). Genome Biol. 9, R137.

Zhou, P., Blain, A.E., Newman, A.M., Zaka, M., Chagaluka, G., Adlar, F.R., Offor, U.T., Broadbent, C., Chaytor, L., Whitehead, A., et al. (2019). Sporadic and endemic Burkitt lymphoma have frequent FOXO1 mutations but distinct hotspots in the AKT recognition motif. Blood Adv. 3, 2118–2127.

STAR★METHODS

KEY RESOURCES TABLE

REAGENT or RESOURCE	SOURCE	IDENTIFIER
Antibodies		
Rabbit monoclonal anti-FOXO1 (clone C29H4)	Cell Signaling Technology	2880; RRID:AB_2106495
Rabbit monoclonal anti-p-AKT (S473) (clone 14-5)	Dako	M3628
HRP Labeled Polymer Goat Anti-Rabbit	Dako	K4002
Rabbit monoclonal anti p-FoxO1 (T24)/FoxO3a(T32)/ FoxO4(T28) (clone 4G6)	Cell Signaling Technology	2599; RRID:AB_2106814
Mouse monoclonal anti-FOXO1(clone D8T1S)	Cell Signaling Technology	97635; RRID:AB_2800285
Rabbit monoclonal anti-p-AKT (S473) (cloneD9E)	Cell Signaling Technology	4060; RRID:AB_2315049
Rabbit monoclonal anti-p-JNK/SAPK (T183/Y185) (clone 81E11)	Cell Signaling Technology	4668; RRID:AB_823588
Rabbit poluclonal anti- p-ATF2 (T71)/pATF7 (T53)	Cell Signaling Technology	24329
Rabbit monoclonal anti-p-p38 (T180/Y182) (clone D3F9)	Cell Signaling Technology	4511; RRID:AB_2139682
Rabbit monoclonal anti AKT (clone C67E7)	Cell Signaling Technology	4691; RRID:AB_915783
Rabbit polyclonal anti-JNK/SAPK	Cell Signaling Technology	9252; RRID:AB_2250373
Rabbit monoclonal anti-ATF2 (D4L2X)	Cell Signaling Technology	35031; RRID:AB_2799069
Rabbit monoclonal anti p38 MAPK (D13E1)	Cell Signaling Technology	8690; RRID:AB_10999090
Rabbit monoclonal anti- p-ERK1/2 (T202/Y204) (clone 197G2)	Cell Signaling Technology	4377; RRID:AB_331775
Rabbit polyclonal anti-ERK	Cell Signaling Technology	9102; RRID:AB_330744
Mouse monoclonal anti-ACTIN	Sigma-Aldrich	A5441; RRID:AB_476744
Mouse monoclonal anti-TUBULIN (clone DM1A)	Cell Signaling Technology	3873; RRID:AB_1904178
Rabbit polyclonal anti-PHLPP1	Bethyl Laboratories	A300-660A; RRID:AB_2283757
Rabbit polyclonal anti-FOXO1A (ChIP Grade)	Abcam	39670; RRID:AB_732421
Rabbit monoclonal anti-CD21 (clone EP3093)	Abcam	75985; RRID:AB_1523292
Rat monoclonal anti-AID (clone mAID-2)	eBioscience	14-5959-82; RRID:AB_10669583
Rabbit monoclonal anti-BCL6 (clone D65C10)	Cell Signaling Technology	5650; RRID:AB_10949970
Rabbit monoclonal anti-ATF-2 (clone D4L2X) (IHC/IF)	Cell Signaling Technology	35031; RRID:AB_2799069
Rabbit monoclonal anti- p-ATF2 (T71)/ATF-7 (T53)(clone E4A5G) (IHC/IF)	Cell Signaling Technology	27934
Rabbit monoclonal anti-Ki67 (clone D3B5)	Cell Signaling Technology	12202S; RRID:AB_2620142
Rat monoclonal anti-B220 (clone RA3-6B2) (IHC)	eBioscience	14-0452-82; RRID:AB_467254
PNA-Biotin	Vector Laboratories	B-1075; RRID:AB_2313597
Rat monoclonal anti-B220 (clone RA3-6B2)	eBioscience	45-0452-82; RRID:AB_1107006
Hamster monoclonal anti-CD95/Fas (mouse) (clone Jo2)	BD Biosciences	557653; RRID:AB_396768
Rat monoclonal anti-GL7 anti (hu/mo) (clone GL7)	eBioscience	53-5902-82; RRID:AB_2016717
Rat monoclonal anti-CD86 (mouse) (clone B7-2)	eBioscience	17-0862-81; RRID:AB_469418
Rat monoclonal anti-CXCR4 (mouse/hu) (clone 2B11)	eBioscience	48-9991-82; RRID:AB_2574143
Mouse monoclonal anti-p-JNK (T183/Y185) (human/mouse) (clone N9-66)	BD Biosciences	562480; RRID:AB_11153134
Rabbit monoclonal anti-p-ATF2 (clone 11G2)	Cell Signaling Technology	13850
Rabbit monoclonal anti-p-AKT (clone D9E)	Cell Signaling Technology	5315; RRID:AB_10694850
Rat monoclonal anti-CD21/CD35 (clone 7E9)	Biolegend	123419; RRID:AB_1953276
Rat monoclonal anti-CD23 (clone B3B4)	Biolegend	101615; RRID:AB_2103307
Rat monoclonal anti-PD-1 (clone 29F.1A12)	Biolegend	135205; RRID:AB_1877232
Rat monoclonal anti-CXCR5 (clone L138D7)	Biolegend	145513; RRID:AB_2562208

(Continued on next page)

Continued

REAGENT or RESOURCE	SOURCE	IDENTIFIER
Rat monoclonal anti-IgM (mouse) (clone RMM-1)	Biolegend	406507; RRID:AB_315057
Rat monoclonal CD93 (mouse) (clone AA4.1)	Biolegend	136509; RRID:AB_2275879
Rat monoclonal anti-CD3 (clone 17A2)	Biolegend	100203; RRID:AB_312660
Rat monoclonal anti-CD4 (clone RM4-4)	Biolegend	116013; RRID: AB_2563024
Mouse monoclonal anti-CD45.1 (mouse) (clone A20)	eBioscience	48-0453-82; RRID:AB_1272189
Rabbit polyclonal anti histone H3	Bethyl Laboratories	A300-823A; RRID:AB_2118462
Rabbit monoclonal anti-p-Ikba (S32) (clone 14D4)	Cell Signaling Technology	2859; RRID:AB_561111
Mouse monoclonal anti-Ikba (clone L35A5)	Cell Signaling Technology	4814; RRID:AB_390781
Mouse monoclonal anti-CD95/Fas (human) (clone DX2)	BD Biosciences	747413; RRID:AB_2872101
Rat anti-Cd16/Cd32 (TruStain fcX, mouse) (clone 93)	Biolegend	101320; RRID:AB_1574975
Rabbit IgG, polyclonal Isotype Control (ChIP-Seq)	Abcam	37415; RRID:AB_2631996
Rabbit monoclonal anti-Cleaved Caspase-3 (Asp175) (clone D3E9)	Cell Signaling Technology	9602; RRID:AB_2687881
Digital Goat anti-Rabbit-HRP	Kindle Biosciences	R1006; RRID:AB_2800464
Digital Goat anti-mouse-HRP	Kindle Biosciences	R1005; RRID:AB_2800463
Cy3-AffiniPure F(ab')2 Fragment Donkey Anti-Rabbit IgG (H+L)	Jackson ImmunoResearch	711-166-152; RRID:AB_2313568
Bacterial and virus strains		
Stable competent E.Coli	New England Biolabs	C3040H
10-beta competent E.coli	New England Biolabs	C3019H
Chemicals, peptides, and recombinant proteins		
Cal-101	Chayman Chemical	15279
SP600125	AdooQ Bioscience	129-56-6
JNK-IN8	AdooQ Bioscience	A12749
LY294002	Cayman Chemical	70920
GDC-0941 (Pictilisib)	Selleckchem	S1065
anti-human IgG + IgM goat polyclonal	Jackson ImmunoResearch Laboratories	109-005-044
Goat Anti-Mouse IgM, u chain specific	Jackson ImmunoResearch Laboratories	115-006-020
MegaCD40L (human)	Enzo Life Sciences	ALX-522-110-C010
anti-mouse CD40 (clone HM40-3)	Invitrogen	16-0402-85 (RRID AB_468946)
DAPI Solution	Thermo Fisher Scientific	62248
fluoromount-G	Electron Microscopy Services	17984-25
Magna ChIP Protein A+G Magnetic Beads	Millipore Sigma	16-663
Cell Proliferation Dye eFluor 450	eBioscience	65-0842-85
KwikQuant Ultra Digital-ECL Substrate Solution	Kindle Biosciences	R1002
ImmPRESS Polumer Anti-rabbit IgG Reagent	Vector Laboratories	MP-7401
TSA Plus Cyanine 3	Perkin Elmer	NEL744001KT
Cytofix/Cytoperm Fixation/Permeabilization	BD Bioscience	BD554714
NcoI-HF Restriction Enzyme	New England Biolabs	R3193
Pierce Protease and Phosphatase Inhibitor	Thermo Fisher Scientific	A32961
Biotin-binder Dynabeads	Life Technologies	#11047
Lenti-X concentrator	Clonetech	631231
TRIzol LS Reagent	Thermo Fisher Scientific	10-296-010
Retro-X Concentrator	Clonetech	631456
Recombinant Murine IL-3	Peprotech	213-13
Recombinant Murine IL-4	Peprotech	214-14-20
Recombinant Murine IL-6	Peprotech	216-16

Continued

REAGENT or RESOURCE	SOURCE	IDENTIFIER
Murine SCF	Peprotech	250-03
Hexadimethrine Bromide (Polybrene)	Sigma-Aldrich	H9268
Neomycin Sulfate	Goldbio	N-620-100
DietGel 76A	ClearH20	72-07-5022
Goat Normal Serum	Jackson ImmunoResearch Laboratories	005-000-121
Critical commercial assays		
2x SYBR Green qPCR Master Mix	BiMake	B21202
Avidin/biotin Blocking Kit	Vector Laboratories	SP-2001
Bolt 4-12% Bis-Tris Gels	Thermo Fisher Scientific	NP0321
Genomic Tail Lysis Kit	BiMake	B40013
Gibson Assembly Master Mix	New England Biolabs	E2611
Kapa Hifi Hotstart	Roche	KK2501
MagniSort Mouse B Cell Enrichment	Life Technologies	8804-6827-74
MicroTube for Sonication	Diagenode	C30010010
Nano-Glo Dual Luciferase Reporter Assay	Promega	N1610
NEBNext NGS DNA Library Preparation	New England Biolabs	E7500, E7645
PureLink RNA Mini Kit	Thermo Fisher Scientific	12183018A
SignalStain Antibody Diluent	Cell Signaling Technologies	8112S
SignalStain Boost IHC Detection Reagent (HRP, Rabbit)	Cell Signaling Technologies	8114S
SuperScript IV VILO Master Mix	Thermo Fisher Scientific	11756050
Universal Plus mRNA-Seq	Nugen	0508-32
Vectastain ABC AP Detection kit	Vector Laboratories	AK-5000
Vector Blue Substrate kit, AP	Vector Laboratories	AK-5300
Zenon Rabbit IgG Labeling Kit	Thermo Fisher Scientific	Z25352
2x SYBR Green qPCR Master Mix	BiMake	B21202
Deposited data		
RNA-Seq and ChIP-Seq raw and processed data, Wildtype and FOXO1 mutant SUDHL4 clones	This study	Gene Expression Omnibus (GEO) GSE143775
H3K27ac ChIP-seq track (SUDHL4 cells)	PMID: 31519498	Gene Expression Omnibus (GEO) GSE132365
Human reference genome NCBI build 37, GRCh37	Genome Reference Consortium	http://www.ncbi.nlm.nih.gov/projects/genome/assembly/grc/human/
Gene expression datasets DEC205+ positively selected cells	Ersching et al., 2017	Gene Expression Omnibus (GEO), record GSE98778
Gene expression datasets, MYC+ GC B cells	Dominguez-Sola et al., 2012	Gene Expression Omnibus (GEO), record GSE38304
DLBCL Patient Dataset #1	Schmitz et al., 2018	dbGaP phs001444
DLBCL Patient Dataset #2	Arthur et al., 2018; Ennishi et al., 2019	ega-archive EGAS00001002657
Experimental models: Cell lines		
Human: HEK293T/17	ATCC	CRL-11268
Human: SU-DHL-4	DSMZ	ACC 495
Human: SU-DHL-10	DSMZ	ACC 576
Human: OCI-LY7	DSMZ	ACC-688
Experimental models: Organisms/strains		
Mouse: B6.SJL	The Jackson Laboratory	JAX: 002014
Mouse: GFP-c-Myc KI	The Jackson Laboratory	JAX: 21935

(*Continued on next page*)

Continued

REAGENT or RESOURCE	SOURCE	IDENTIFIER
Mouse: B6.Foxo1M1L mice	This study (see STAR Methods)	N/A
Mouse: C57BL6/J	The Jackson Laboratory	JAX: 000664
Mouse: IghelMD4	The Jackson Laboratory	JAX: 002595
Oligonucleotides		
ssODN CRISPR targeting mouse embryos (M1 > L): GGAGCGACACTCGGGTCGCC CGCTCCGCGCCCCCGGTGGCCGCGTC TCCCGGTACTTCTCTGCTGGTGGGGG AGGGGCGGGGGCAaCtTGGCCGAAG CGCCCCAGGTGGTGGAGACCGAC CCGGACT	This study	N/A
guide RNA sequence for mouse FOXO1 M1 > L targeting: CACCTGGGGCGC TTCGGCCA	This study	N/A
Primer, T7 endonuclease assay; MmFoxo1-E1-T7-F1: GGTGACCCAGCGAAGTTAAG	This study	N/A
Primer, T7 endonuclease assay; MmFoxo1-E1-T7-R1: GATGGCCTTGGTGATGAGGT	This study	N/A
guide RNA human FOXO1, Met 1 targeting: GGCGGGGGTCACCATGGCCG	This study	N/A
guide RNA human FOXO1 Ser 22 and Thr 24 targeting: CGGACTTCGAGCCGCTGCCC	This study	N/A
guide RNA human FOXO1, 5′ end for null allele: GAGCAACCTGAGCTTGCTGG	This study	N/A
guide RNA human FOXO1, 3′ end for null allele: GGAGAGCGAGGACTTCCCGC	This study	N/A
ssODNs CRISPR donor, human FOXO1 M1L: GTTCTCCCCCTCTTGGCTC TCCTGCGGCTGGGGGAGGGGCGGG GGTCACCcTtGCCGAaGCGCCTCAGG TGGTGGAGATCGACCCGGACTTCGA GCCGCTGCCCCGGCC	This study	N/A
ssODNs CRISPR donor, human FOXO1 T24I: CGGCGTCGGGGTTGGCAGCC GCGCTGCCCGACGGCGCCGGGCTG GAGGTGGCCGAGTTGGACTGGCTA AACTCCGGCCTGGGCAGCGGCCAG aTGCACGAGCGCGGaCGGGGCAGCGG CTCGAAGTCCGGGTCGATCTCCACCAC	This study	N/A
ssODNs CRISPR donor, human FOXO1 S22P: CGGGGTTGGCAGCCGCGCTGC CCGACGGCGCCGGGCTGGAGGTGG CCGAGTTGGACTGGCTAAACTCCGG CCTGGGCAGCGGCCAGGTGCACGgGC GCGGaCGGGGCAGCGGCTCGAAGTC CGGGTCGATCTCCACCAC	This study	N/A
Primer, T7 endonuclease assay; HsFOXO1_T7 Primer_F: GAGGAGCCTCGATGTGGATG	This study	N/A
Primer, T7 endonuclease assay; HsFOXO1_T7 Primer_R: GAGTCCACTCACCTTCCAGC	This study	N/A
Primer: SUDHL4 T7 cut sequencing_R: TGCGGGAAGTCCTCGCTCTC	This study	N/A
shRNA control (Renilla Luciferase): TATCATTAACTGTTTCTCTGTA	This study	N/A

Continued

REAGENT or RESOURCE	SOURCE	IDENTIFIER
shRNA human PHLPP1 #1: TTACATATCTGATATGTTAGGG	SplashRNA tool http://splashrna.mskcc.org	N/A
shRNA human PHLPP1 #2: TATCATTAACTGTTTCTCTGTA	SplashRNA tool http://splashrna.mskcc.org	N/A
shRNA human FOXO1 #5275: TATAAATTAAGAACTCTTAGGA	SplashRNA tool http://splashrna.mskcc.org	N/A
qPCR primer PHLPP1 F: TGCTCACTCCAACTGCATCGAG	Origene Technologies	#HP219264
qPCR primer PHLPP1 R: GGTTTCCAGTCAGGTCTAGCTC	Origene Technologies	#HP219264
qPCR primer TBP F: TAATCCCAAGCGATTTGCTG	PMID 28092697	N/A
qPCR primer TBP R: CAGTTGTCCGTGGCTCTCTT	PMID 28092697	N/A
qPCR primer POL2RA F: AAGTTCAACCAAGCCATTGCG	PMID 25526394	N/A
qPCR primer POL2RA R: GACACACCAGCATAGTGGAAGG	PMID 25526394	N/A
Primer: Mouse IGH VDJ, segment VH7183-F: GCAGCTGGTGGAGTCTGG	PMID: 15994971	N/A
Primer: Mouse IGH VDJ, segment VHQ52-F: TCCAGACTGAGCATCAGCAA	PMID: 15994971	N/A
Primer: Mouse IGH VDJ, segment JH4E-R: AGGCTCTGAGATCCCTAGACAG	PMID: 7953531	N/A
Recombinant DNA		
RT3-REVIR	PMID: 29568061 A gift from Johannes Zuber	Addgene plasmid # 111168
pHRSIN-dE-SFFV-GFP-P2A-SBP-dLNGFR-WPRE	Matheson et al., 2014	N/A
pMSCV Vector	PMID 20008935 A gift from Lin He	Addgene plasmid # 24828
pCL-Eco	PMID 8764092 A gift from Inder Verma	Addgene plasmid # 1237
pMD2.VsVg	A gift from Didier Trono	Addgene plasmid # 12259
psPAX2	A gift from Didier Trono	Addgene plasmid # 12260
pNL3.1 (Nluc-min) Nanoluc Luciferase vector	Promega	#N1031
pX330-U6-Chimeric_BB-CBh-hSpCas9	PMID 23287718 A gift from Feng Zhang	Addgene plasmid # 42230
pcDNA3-FOXO1 (WT and variants)	This study	pcDNA3 backbone originally purchased from Invitrogen
Software and algorithms		
ImageJ V 2.0.0	Rueden et al., 2017	https://imagej.nih.gov/ij/
MACS version 2.1.1.20160309	Zhang et al., 2008	https://github.com/taoliu/MACS
HOMER V 4.8	Heinz et al., 2010	http://homer.ucsd.edu/homer/
DeepTools2.0	Ramírez et al., 2016	https://deeptools.readthedocs.io/en/develop/index.html
Python version 3.0	Python Software Foundation	https://www.python.org
GSEA v 4.0	Subramanian et al., 2005	https://software.broadinstitute.org/gsea/index.jsp
DESEQ2	Love et al., 2014	http://bioconductor.org/packages/devel/bioc/vignettes/DESeq2/inst/doc/DESeq2.html

Continued

REAGENT or RESOURCE	SOURCE	IDENTIFIER
HierarchicalClusteringV8	Genepattern Server	https://cloud.genepattern.org/gp/pages/protocols/ClassDiscovery_hier.html
LEM (Leding Edge Metanalysis)	Godec et al., 2016	https://github.com/lamarck2008/LEM
QuPath v 0.1.2	Bankhead et al., 2017	https://qupath.github.io/
NIS Elements software	Nikon	https://www.microscope.healthcare.nikon.com/products/software/nis-elements
SplashRNA Algorithm	Pelossof et al., 2017	http://splashrna.mskcc.org/
Voom Normalization	Law et al., 2014	https://rdrr.io/bioc/limma/man/voom.html
FlowJo (V10.5.3)	BD Bioscience	https://www.flowjo.com/
tophat/2.1.0	Trapnell et al., 2009	https://ccb.jhu.edu/software/tophat/index.shtml
cufflinks/2.2.1	Trapnell et al., 2010	http://cole-trapnell-lab.github.io/cufflinks/
HTSeq	Anders et al., 2014	https://htseq.readthedocs.io/en/release_0.11.1/
samtools/0.1.19	Li et al., 2009	http://samtools.sourceforge.net/
bowtie2/2.2.8	Langmead and Salzberg, 2012	http://bowtie-bio.sourceforge.net/bowtie2/index.shtml
ggsurvplot / ggplot2 (survminer R package)	https://doi.org/10.1007/978-0-387-98141-3	https://github.com/kassambara/survminer/
Illustrator 2021	Adobe Systems Inc.	N/A
Photoshop 2021	Adobe Systems Inc.	N/A
Prism 9	Graphpad	https://www.graphpad.com/scientific-software/prism/
Other		
CFX384 Real-Time PCR Detection System	BioRad	1855484
X-A2 Digital Camera	FujiFilm	N/A
DynaMag-2	Thermo Fisher Scientific	12321D
Eclipse E200 Microscope	Nikon	N/A
Neon Transfection Kit	Invitrogen	MPK5000
LSRII-Aria Cell Sorter	BD	N/A
LSRFortessa Analyzer	BD	N/A
FACSCalibur Analyzer	BD	N/A
Bioanalyzer 2100	Agilent	N/A

RESOURCE AVAILABILITY

Lead contact
Further information and requests for resources and reagents should be directed to and will be fulfilled by the lead contact, David Dominguez-Sola (david.dominguez-sola@mssm.edu).

Materials availability
Plasmids and viral vectors generated in this study will be deposited in Addgene. In the meantime, these reagents will be made available upon reasonable request.

The B6.Foxo1M1L mouse line, and SUDHL4 isogenic FOXO1 mutant cell lines generated in this study are available upon request.

Data and code availability
All RNA-seq and ChIP-seq datasets have been deposited in the Gene Expression Omnibus (GEO) database under accession number GSE143775 (reference series).

The modified computational pipeline for Leading Edge Metanalysis, updated to run in Python3, is available from the corresponding author upon request. All Western Blot raw images have been deposited in Mendeley Data: https://data.mendeley.com/datasets/xfv7v9k45r/1.

EXPERIMENTAL MODEL AND SUBJECT DETAILS

Mouse strains

All mice used in this study were in pathogen-free conditions, at 22°C and 30%–70% humidity in a 12-h light/dark cycle and provided *ad libitum* access to food and water. All experiments conformed to the ethical principles and guidelines of our Institutional Animal Care and Use Committee at Mount Sinai (IACUC approval number 2014-0015). CD45.1 B6 congenic mice (B6.SJL-*Ptprc^a^ Pepc^b^*/BoyJ) were purchased from the Jackson Laboratory (#002014). The Myc-GFP mice (GFP-c-Myc KI, *B6;129-Myc^tm1Slek^/J*; Jackson Laboratory #021935) were a kind gift of Dr. Barry P. Sleckman (Huang et al., 2008). MD4 mice (C57BL/6-Tg(IghelMD4)4Ccg/J), which express a transgenic B cell receptor specific for hen egg lysozyme, were purchased from the Jackson Laboratory (#002595). B6.IghelMD4 and congenic CD45.1/2 mice were bred in house.

All materials, including IVCs, lids, feeders, bottles, bedding, and water were autoclaved before use. Same sex litter mates were housed together in individually ventilated cages, up to five per cage. Male and female mice were aged 8-12 weeks at the start of experiments unless otherwise stated. Sample sizes were not calculated *a priori*. Given the nature of the comparisons, we did not randomize mice into experimental groups or blind the investigators to group allocation.

Cell lines

SUDHL4 (DSMZ # ACC 495) and SUDHL10 (DSMZ # ACC 576) cell lines were a kind gift of the laboratory of Dr. Riccardo Dalla-Favera (Columbia University Medical Center, New York, NY, USA). The OCI-LY7 cell line was purchased from DSMZ-German Collection of Microorganisms and Cell Cultures GmbH (cat #ACC-688). All stocks were frozen after 2-3 passages. SUDHL4, SUDHL10 and OCI-LY7 are wild-type for FOXO1 DLBCL, GCB-like). The identity of all cell lines and SUDHL4 isogenic clones was confirmed by multiplex cell authentication (Genetica Cell Line Testing). The cytogenomic analysis of SUDHL4 parental and CRISPR-edited isogenic lines was done at the Mount Sinai Tumor Cytogenomics core. All cell lines were cultured in Iscove Modified Dulbecco's Medium (IMDM; Life Technologies, Cat #12440-061) supplemented with 10% fetal bovine serum (FBS, Invitrogen #10437) and 1% Penicillin/Streptomycin (Life Technologies, Cat #15140163).

Human tissue samples

Fresh tonsil tissues were obtained from routine tonsillectomies at the Children's Hospital of Columbia- Presbyterian Medical Center or the Mount Sinai Hospital. All samples were exempt from the requirement for informed consent as they corresponded to residual material obtained after diagnosis, from anonymous donors without identification of samples, in compliance with Regulatory Guideline 45 CFR 46.101 (b)(4) for Exempt Human Research Subjects of the US Department of Health and Human Services and with protocols approved by the Institutional Ethics Committee. Deidentified paraffin sections of tonsils correspond to archived tissues after diagnosis in the Department of Pathology at Mount Sinai Hospital, New York. These samples are in compliance with Regulatory Guideline 45 CFR 46.101 (b)(4) for Exempt Human Research Subjects of the US Department of Health and Human Services.

METHOD DETAILS

Generation of Foxo1 M1L mice

The *B6.Foxo1^M1L^* mouse line was generated by CRISPR-Cas9-directed gene editing C57BL/6 zygotes. Briefly, we injected Alt-R Cas9 ribonucleoprotein complexes, made of Alt-R Cas9 Nuclease 3NLS, and annealed active guide RNA (crRNA⁺tracrRNA at a 1:1 ratio), and a single-strand oligonucleotide donor (ssODN) containing the p.Met1 < Leu mutation into one-cell stage C57BL/6 zygotes (20 ng/μL of guide RNA and 20 ng/μL of Cas9 protein and 20ng/uL ssODN), following the manufacturer's protocol (Integrated DNA Technologies, Coralville, IA, USA). Guide RNA and ssODN donor sequences were designed using the DESKGEN CRISPR tool (http://www.deskgen.com; Desktop Genetics Ltd.). We discarded guide RNAs with poor off-target scores and tested 3 potential candidate guides for their activity. We chose a guide RNA with cut site at chr3 [+52,268,805:-52,268,805]; GRCm38.81), [5′CACCTGGGGCGCTTCGGCCA3′]. This guide cut 1nt from the p.Met1 codon, and no predicted off-targets located in coding regions and a single predicted off-target with 2 mismatches located at chr11: 78153102-78153125, in an intronic segment of the KCTD21-AS1 gene. We designed an asymmetric ssODN donor (36/91 bp arms) that included an ATG > TTG mutation, equivalent to the pMet1 > Leu mutation observed in B-NHL, and a second mutation to abrogate the PAM site, here in lowercase (GGCAaCtTGGCC; start codon is underlined). Additionally, these two mutations destroy a *NcoI* restriction site, which was used for genotyping. The successful targeting frequency was of 15% (heterozygous founders) and 5% (homozygous). We crossed selected founders to C57BL/6 mice and confirmed germline transmission for 4 of them. All mice used in this manuscript were derived from two separate founders. Mutant founders were identified by digestion with NcoI-HF (New England Biolabs) of PCR products containing the targeted region (see below), and further validated by Sanger sequencing (Eton Bioscience, USA). Offspring and experimental animal cohorts were genotyped by qPCR (Transnetyx). Primers used for sequencing can be found in the Key resources table.

Heterozygous and homozygous *Foxo1*^M1L^ mice were born at normal Mendelian ratios and had normal lifespans (median follow-up = 78 weeks, range 62-88 weeks). Additional phenotypic details are described in Figure S7.

Mouse immunizations

To induce T cell dependent immune responses, we immunized 8 to 12-week-old mice with Sheep red blood cells (SRBCs, Cocalico Biologicals #20-1334A) twice (day 0, 2x10^8 SRBCs and day 5, 1x10^9 SRBCs) by intraperitoneal injection and analyzed at day 12 (Compagno et al., 2017). SRBCs had been washes and resuspended in 0.25 mL of 1X PBS. Age and sex matched C57BL/6J mice were used as controls in some cases (the Jackson Laboratory, #000664). An equal percentage of male and females were included in all experiments. Immunizations and downstream analyses were performed by separate investigators.

Generation of FOXO1 mutant SUDHL4 cells via CRISPR/Cas9 targeting
sgRNA and ssODN designs

All guide RNAs and ssODN donors were designed using the DeskGen CRISPR tool (Desktop Genomics Ltd). We used the same guide RNA to generate clones carrying T24 and S22 mutations (5'CGGACTTCGAGCCGCTGCCC3'). This guide RNA directs Cas9 to cut ~18nt 5' of T24 site, and 12nt 5' of S22 chr13 [+40,666,161: −40,666,161; GRCh38]. The cut is > 10nt away from the substitution site, but other guides with closer cuts performed poorly in T7 assays or had too many predicted off-target sites. This guide RNA has no predicted off-target effects with less than 3 mismatches in coding or non-coding regions. For HDR-mediated repair, we provided an asymmetric (36/91) ssODN donor that contained a mutated PAM sequence (CGG to CGT, silent mutation at p.Arg19, R19).

To introduce Met1 > Leu (M1L) mutation, we selected one gRNA with PAM at p.Glu3 (5'GGCGGGGGTCACCATGGCCG3'). This sgRNA has one predicted off-target mapping at exon 14 of the ARHGEF17 gene [chr11: 73362603-7336262], with 2 mismatches within seed region. Four additional off-targets were predicted within coding regions, all with 3 mismatches; and 4 with 2 seed mismatches predicted to target non-coding sequences. The ssODN donor was designed to mutate methionine 1 (M1) to Leucine (ATG > CTT), equivalent to the mutations found in DLBCL. We also added a silent point mutation at p.Glu3 (PAM region), from GAG to GAA. FOXO1 sgRNAs were subcloned into a modified vector backbone based on the pX330 plasmid (pX330-U6-Chimeric_BB-CBh-hSpCas9, a gift from Feng Zhang (Cong et al., 2013; Ran et al., 2013) (Addgene plasmid # 42230 ; http://n2t.net/addgene:42230 ; RRID:Addgene_42230), altered to introduce a eGFP-Puromycin-P2A cassette in-frame 5' to Cas9 (pX330-Cas9-eGFP; a gift of Aleksandra Oblewska and Brian Brown, Icahn School of Medicine at Mount Sinai). All guide RNAs were subcloned between two BbsI sites. GFP expression was used to identify successfully electroporated cells.

To generate FOXO1 null (KO) SUDHL4 isogenic clones, we designed two guide RNAs targeting FOXO1 after p.Met71, preventing usage of this methionine as alternative translation start site: sg1: 5'GAGCAACCTGAGCTTGCTGG3'; sg2: 5'GGAGAGCGAGG ACTTCCCGC3' (directed cleavage around residues 77 and 84, respectively). These two guides had no predicted off-target sites in coding regions with less than 3 seed mismatches. Both guide RNAs were combined during electroporation without donor ssODN.

Electroporation

GFP-Cas9-gRNA containing plasmids and ssODN donors were mixed at a 1:50 molar ratio. Per electroporation, 7.6x10^5 SUDHL4 cells were resuspended in 100 uL of R buffer and 5 ug total DNA electroporated using a Neon device (Life Technologies/ThermoFisher) using manufacturer's instructions and the following conditions: 1350 V; 1 pulse; 30 ms in a 100 uL tip. Three independent electroporations were pooled per well. After electroporation cells were cultured in IMDM/10% FBS without antibiotics for 24 to 48 h in 5% CO2 incubator at 37°C.

Single cell sorting via Flow Cytometry.

To enrich for targeted clones, SUDHL4 single cells were resuspended in complete growth medium and sorted into individual wells based on viability (7-AAD exclusion) and GFP expression using LSRII-Aria Cell Sorter (Beckton-Dickinson) with a 96-well plate automated stage. One cell was seeded in a well containing 100 uL of IMDM/10% FBS + Pen/Strep (96-well plate). A range of 200-400 single-cells were seeded per variant. Single cell clones were expanded and screened for correct targeting by restriction digestion first, then Sanger sequencing. For M1L clones, successful editing was further confirmed by Western Blot using FOXO1 specific antibodies. In parallel, we generated SUDHL4 wild-type isogenic controls from the parental SUDHL4 lines by serial dilution and expansion of single cells in 96-well dishes. Four randomly selected clones were used in most experiments, as detailed in the figure legends.

Immunoblot analyses

For cell lysis, we used 1% SDS lysis buffer (50 mM Tris, pH 8.0, 1 mM EDTA, 100 mM NaCl, 5 mM DTT, and 1% SDS) containing protease and phosphatase inhibitors (Thermo Fisher Scientific). Protein lysates were resolved in Novex Bolt 4%–12% Bis-Tris gels (Life Technologies/Thermo Fisher Scientific) and transferred to nitrocellulose membranes. All membranes were blocked with 5% milk in TBS-T (Tris-buffered saline with 0.1% Tween) for 1 h at room temperature and incubated overnight at 4C with various primary antibodies diluted in TBS-T plus 3% BSA (see supplemental materials), washed 3 times in TBS-T, then incubated with horseradish peroxidase-conjugated secondary antibodies (Kindle Biosciences #K1005, #K1006) and developed using KwikQuant Ultra Digital ECL (Kindle Biosciences #K1002). Luminescent signals were detected using a FujiFilm X-A2 digital camera. Raw images were then converted to black and white using Adobe Photoshop CS6 V13.0.6.

Cell fractionation and isolation of chromatin enriched fractions

After harvesting, we washed cells once in cold PBS with protease and phosphatase inhibitors (Thermo Fisher Scientific), then resuspend in CSK buffer (10mM HEPES-Na, pH7.9, 100 mM NaCl, 1.5 mM MgCl$_2$, 300 mM sucrose, and 0.5% Triton X-100) with protease

and phosphatase inhibitors, then incubated for 10 min on ice. Nuclear pellets were collected by centrifugation (5000 rpm, 5 min at 4°C). We then washed the pellets twice in CSK buffer and resuspended in EDTA-EGTA buffer (20 mM HEPES-Na, pH 8.0, 3 mM EDTA, 0.2 mM EGTA, 50 mM NaF, 0.1 mM Na_3VO_4) with protease and phosphatase inhibitors, followed by a short incubation (4 min on ice), and centrifugation (5000 rpm, 3 min at 4°C). We washed the resulting pellets twice in the same EDTA-EGTA buffer, to obtain a compact chromatin-enriched pellet. These pellets were flash-frozen and stored at −80°C until processing for immunoblot.

Flow cytometry analyses

Mononuclear cells or enriched B cell fractions were stained in FACS (1X PBS, 0.5% BSA, 2 mM EDTA buffer) with specific combinations of fluorescent-labeled antibodies. We used DNA dyes and physical parameters to exclude non-viable cells. For intracellular phospho staining for flow cytometry analysis, we first stained for cell-surface markers in FACS buffer; then fixed and permeabilized these cells by incubating in BD Cytofix/Cytoperm™ Buffer (BD #554722) for 30 min on ice. Cells were washed in 1x BD Perm/Wash Buffer (#554723) and incubated with BD Cytoperm Permeabilization Buffer Plus for 10 min on ice; washed again with BD Cytofix/Cytoperm™ Buffer, re-fixed with BD Cytofix/Cytoperm Buffer (5 min on ice), washed again in 1x BD Perm/Wash Buffer and then finally labeled with phospho-specific antibodies diluted in 1x BD Perm/Wash Buffer at room temperature for 1 h. We then washed the cells twice 1x BD Perm/Wash Buffer and resuspend all samples in flow cytometry buffer. We acquired > 1 million events per mouse using a FACSCalibur or BD Fortessa (BD Bioscience). We used FlowJo software, Mac version v10.5.3 (Flowjo LLC, BD) for data analysis. The antibodies used for flow cytometry as listed in the Key resources table.

Cell isolation with Streptavidin-Binding-Peptide for cell competition studies

To generate differentially labeled cell pools for cell competition experiments, we first transduced SUDHL4 cells (FOXO1 wild-type or FOXO1 mutant isogenic clones) with pHRSin-GFP-LNGFR-SBP (FOXO1 wild-type or mutant) or pHRSin-mCherry-LNGFR-SBP (wild-type) lentiviral particles. The expression of a non-functional dLNGFR receptor fused to Streptavidin binding peptide (SBP) (Matheson et al., 2014) allows to enrich at purity for successfully transduced cells using Biotin-binder Dynabeads (Life Technologies, #11047). The volume of streptavidin beads used was proportional to the number of GFP+ or mCherry+ cells after transduction. We washed all cells three times with *Incubation Buffer* (IB: PBS without calcium/magnesium, 2 mM EDTA, Biotin-free 0.1% BSA), resuspended them (10^7cells/ml in IB buffer) and incubated the cell suspension with Dynabeads (20:1 bead:target-cell ratio) rotating for 30 min at 4°C. Bead-bound cells were captured using a DynaMag2 magnet (Invitrogen) (2–3 minute incubation). SBP+ cells were released by resuspending pre-warmed "release" buffer (IMDM/10% FBS supplemented with 25 mM biotin) and incubating for 15 min at room temperature while rotating. We collected the released cells from the supernatant, after incubating the suspension in a DynaMag2 magnet. Cell purity was determined by flow cytometry. GFP+/SBP+ or mCherry+/SBP+ cells were seeded in complete medium and recovered for at least 72 h at 37°C before co-culture.

Co-culture assays

Equal numbers of GFP+ and mCherry+ cells (1:1 ratio) were mixed and mixed suspensions washed twice in HBSS and seeded at $5x10^5$ cells/mL in control (IMDM/10% FBS) or starvation medium (HBSS/1% IMDM w/o FBS). Co-cultures were maintained for the indicated times prior to analysis (as detailed in the figure legends). Flow cytometry data acquisition (GFP:mCherry ratios and activated caspase3 content; see below) was done using FACSCalibur or BD Fortessa (BD Bioscience) cytometers. FlowJo software, Mac version v10.5.3 (Flowjo, LLC - BD) was used for data analysis.

Virus packaging and cell transduction

MSCV-based retroviruses were generated by co-transfecting MSCV-based retroviral vectors with the EcoPak plasmid (packaging) at a 1:1 ratio. Lentiviral particles were generated by co-transfecting pHRSin vectors with pMD2.G (VsVg) and psPAX2 (D8.9) plasmids (1:0.25:0.75 ratio, respectively) in HEK293T via reverse transfection with polyethyleneimine (PEI, 15 μg of DNA per 10cm dish, 1:4 DNA:PEI ratio). We collected viral supernatants at 48 and 72 h after transfection, cleared them by centrifugation and 100x concentrated using Retro-X or Lenti-X concentrator (Clontech, # 631231), following manufacturer's instructions. All viral concentrates were stored at −80°C until use. Cells were transduced in the presence of polybrene (4 ug/mL) via spinoculation (2,500 rpm, 32oC, 90 min) twice within at 24-hour period.

Cleaved-caspase3 analysis

SUDHL4 FOXO1 WT and Mutant cells were cultured in competition or as independent cultures in complete medium or starvation (HBSS/1% IMDM) for 6 h with or without PI3K inhibitor CAL101 (20 μM, Cayman Chemical) and JNK inhibitor JNK-IN8 (20 μM, AdooQ Bioscience)). Cells were harvested, washed once in 1x PBS, fixed in 4% paraformaldehyde for 20 min at room temperature, wash once more in 1x PBS and permeabilized in 90% ice cold methanol on ice for 30 min. We washed the cells 3 more times in cold flow cytometry buffer (1X PBS, 0.5% BSA, 2 mM EDTA buffer) and stained with an AF647-conjugated anti-Cleaved Caspase-3 antibody (Cell Signaling Technologies) for 1 h at room temperature. Cells were washed twice and resuspended in flow cytometry buffer. Data were acquired on FACSCalibur or BD Fortessa (BD Bioscience) cytometers and analyzed with FlowJo software, Mac version v10.5.3 (Flowjo, LLC - BD).

Ex-vivo B cell proliferation assays

We isolated enriched B cell fractions from mouse spleens using the MagniSort® Mouse B cell Enrichment Kit (Life Technologies, #8804-6827-74), according to manufacturer instructions. Purified B cells (> 95% purity) were washed with cold PBS and labeled with 10 uM eF450 Cell proliferation dye (eBioscience, #65-0842-85) for 10 min at 37°C. The reaction was then blocked by adding cold B cell medium (RPMI, supplemented with 10% FBS, 0.1 mM nonessential amino acids, 1 mM sodium pyruvate, 50 uM β-mercaptoethanol; Life Technologies) and incubating 5 min on ice. Cells were washed and resuspended in B cell medium at 1×10^{6}/mL, plated in 12 or 6-well plates and stimulated using different cytokine/ligand combinations, as detailed in the legends. Specifically: anti-CD40 (12.5 ng/mL, clone HM-40-3, Life Technologies); mouse IL-4 (20 ng/mL, Peprotech); anti-mouse IgM F(ab)$_2$ (3 ug/mL; Jackson ImmunoResearch); Lipopolysaccharides from *Escherichia coli* O55:B5 (1 ug/mL, Sigma-Aldrich); or anti-mouse CD180 (RP105) (1 ug/mL, Biolegend). In all cases, we stimulated the cells for 72 h before analysis. Dilution of eF450-CPD was assessed by flow cytometry using a BD Fortessa cytometer (BD Bioscience) and data analyzed with FlowJo software, Mac version v10.5.3 (Flowjo, LLC - BD).

Generation of mixed bone marrow chimeras

We isolated total bone marrow cells from the long bones of age and sex matched CD45.1/.2 mice (Jackson Labs) and either FOXO1$^{+/+}$ or FOXO1$^{M1L/M1L}$ CD45.2 mice (~8-10 wks old). After red blood cell lysis (ACK lysis buffer, Lonza) and washes in medium, we mixed these cells at a 1:1 ratio, washed, and resuspended in 1x PBS. A total of five million bone marrow cells were transferred into lethally irradiated recipient 10 wk-old C57BL/6 female mice (CD45.2) via retroorbital injection. All recipient mice had been irradiated with a split dose (5.5 + 5.0 Gy separated 4 h) 24 h prior to cell transfer (RS-2000 small animal irradiator, Rad Source) and were maintained for two weeks in antibiotic drinking water (2g/L Neomycin, Goldbio) and supplemented with nutritionally fortified food (76a DietGel, ClearH2O) after irradiation. Ten weeks post transfer we immunized all mice (d0, d5) with sheep red blood cells (Cocalico Biologicals) and then analyzed at day 12. We used flow cytometry to determine the relative abundance of CD45.1/.2 cells to CD45.2 cells in germinal center (B220+, CD95^{hi}, GL7^{hi}), which was normalized to the ratio in non-GC B cells (B220+, CD95^{lo}, GL7^{lo}) to control for differences in engraftment between mouse haplotypes. A measure of "competitive competency" was defined by normalizing the percentage of CD45.2+ cells within the GC B cell pool (GL7^{hi}/Fas^{hi}) to that in the non-GC naïve B cell compartment, as per previous studies (Basu et al., 2013; Lu et al., 2017).

Adoptive B cell transfer chimeras in IghelMD4 recipient mice

Splenic B cells from age and sex matched CD45.1/.2 mice (Jackson Labs) and either FOXO1$^{+/+}$ or FOXO1$^{M1L/M1L}$ mice were isolated by negative selection (Magnisort Mouse B cell enrichment kit, Life Technologies) and mixed 1:1 in 1x PBS. We then transferred a total of 20 million B cells into recipient IgHEL/MD4 transgenic mice (Jackson Labs) via retroorbital injection. In MD4 mice, > 95% of B cells express a transgenic B cell receptor specific for hen egg lysozyme and fail to recognize NP-peptide conjugates. One day after B cell transfer, we immunized MD4 recipient mice with 100 mg of NP-CGG (Biosearch Technologies) precipitated 1:1 in alum (Alhydrogel; Invivogen). Ten days post immunization, we isolated splenocytes and used flow cytometry to determine the ratio of donor CD45.1/.2 cells to CD45.2 cells in non-germinal center and germinal center (IgDα-, B220+, CD95^{hi}, GL7^{hi}) compartments. The CD45.2 to CD45.1/.2 ratio in donor non-GC B cells (IgDα-, B220+, CD95^{lo}, GL7^{lo}) was used to normalize the germinal center ratios. In our hands, CD45.1/.2 cells were rapidly depleted in IghelMD4 mice after transfer, and this could be alleviated by depleting CD8^{+} T cells with an anti-CD8 (Bioxcell): 200 ug (i.p.) two days before B cell transfer, 100 ug every 4 days after B cell transfer until analysis. We confirmed that this maneuver did not affect normal germinal center responses in C57BL/6 mice. "Competitive competencies" were determined as in the mixed bone marrow chimera experiments described above, as per previous studies (Basu et al., 2013; Lu et al., 2017).

Mouse tumor studies with combined VavP-Bcl2 x Foxo1 transgenes

We isolated and cultured overnight bone marrow cells from two young (11-wk) *VavP-Bcl2* transgenic female mice (Egle et al., 2004), mixed and cultured at 2×10^{6}/mL in B cell medium supplemented with mIL-3 (Peprotech, 10 ng/mL), mIL-6 (Peprotech, 10ng/mL), mSCF (Peprotech, 50ng/mL) and m-Flt3L (Peprotech, 50ng/mL). We then transduced these cells with MSCV-IRES-GFP retroviruses encoding for wild-type FOXO1, Δ70 FOXO1 (N-term 70 aa truncation equivalent to FOXO1 M1L) or only GFP, twice within 24 h by spinoculation (1000 x g, 32°C, 60–90 min) in presence of polybrene (8 ug/mL) at high multiplicity of infection (MOI). The percentage of GFP+ cells upon transduction and prior to injection was ~15%–20% for all samples. These cells were used to reconstitute lethally irradiated 12 wk-old C57BL/6J female recipient mice (1.5 million in 150 uL 1x PBS per mouse — see "mixed bone marrow chimeras" protocol for additional details). Eight weeks after reconstitution, we immunized (i.p.) all mice with 500uL of a 2% suspension of sheep red blood cells in 1x PBS, and re-immunized after 1 month. We analyzed all mice at ~100 days post-reconstitution.

Immunofluorescence analysis of FOXO1 subcellular distribution in cell lines

Cell culture: SUDHL4 cells were seeded in fresh IMDM + 10% FBS at $0.5*10^{6}$ cells/mL with JNK-IN8 (1 uM, AdooQ Bioscience), soluble CD40L (megaCD40L, 100 ng/mL, Enzo Life Sciences), anti-IgM (20ug/mL, Jackson ImmunoResearch), PI3K inhibitor (10 uM, GDC-0941, Selleckchem) or starvation medium (Hanks Buffered Saline Solution + 1% IMDM).

Cytospin preparation and immunofluorescence staining

We adapted a previously described protocol (Richter et al., 2018). Briefly, cells were mixed 1:1 with a 20% sucrose solution in IMDM (or HBSS for serum starvation), then loaded into cytospin funnels (Cytospin 4 device, Thermo Shandon) with pre-wet filters. Cells were centrifuged for 3 min at 800 rpm, then fixed for 20 min at room temperature with a solution containing 3.13% Glyoxal fixative (Sigma-Aldrich), 20% ethanol, 0.75% acetic acid (pH = 4-5). Cytospins were washed in PBS, then blocked/permeabilized in PBS/0.3%BSA/0.3% Triton X-100 for 1 h at room temperature. After overnight incubation with anti-FOXO1 antibody (C29H4, Cell Signaling Technologies, 1:200) at 4°C, slides were washed with PBS-Tween, incubated in ImmPress anti-rabbit secondary antibody for 1 h at room temperature, then washed again in PBS-Tween. Slides were incubated with Tyr-Cy3 reagent (1:1000) (Perkin Elmer) for 3 min, then washed in deionized water, stained with DAPI (Thermo Fisher Scientific), and mounted for image acquisition. All images were captured using a Nikon Eclipse E400 microscope (TRITC/Cy3 filter) and NIS-2000 v2.0 Elements software. For quantification of FOXO1 localization, cells were visually counted as either "mostly nuclear (nuc)," "mixed nuclear/cytoplasmic (mix)" or "mostly cytoplasmic (cyto)." Nuclear FOXO1 scores for each sample were then calculated using the formula: *nuc + 0.5(mix)/ total cell number*.

Immunofluorescence analysis of ATF2 expression in tonsil FFPE sections

For the immunofluorescence analysis of formalin-fixed, paraffin-embedded (FFPE) human tonsils, we used a previously described protocol (Dominguez-Sola and Cattoretti, 2017). Briefly, we prepared 3-μm-thick FFPE sections, which were dewaxed and rehydrated. We then performed heat-induced epitope retrieval in citrate buffer (pH 6.0, + 0.5% Tween) and blocked endogenous biotin using the Avidin-Biotin Blocking Kit (Vector Labs). All tissue sections were further blocked in PBS containing 0.1%Tween, 3% BSA and 5% donkey serum (Jackson ImmunoResearch), followed by incubation overnight at 4°C in a humid chamber with specific antibodies against total ATF-2 protein, or T71-phosphorylated ATF-2 (see Key resources table for details) diluted in SignalStain Diluent (Cell Signaling Technologies). After repeated washes in TBS-0.1% Tween (TBS-T), we incubated the sections for 1 h at room temperature with fluorochrome-conjugated secondary antibodies (donkey anti-rabbit Cy3, Jackson ImmunoResearch), then washed (TBS-T). We next blocked any available anti-rabbit secondary sites with 10% rabbit serum in TBS-T for 1 h at room temperature; and incubated the slides with an anti-CD21 rabbit antibody (2 h at room temperature in a humid chamber), previously labeled with biotin using the Zenon labeling kit (ThermoFisher Scientic), as per manufacturer's instructions. After several washes with TBS-T, we incubated each slide with streptavidin-Alexa405 for 30 min at room temperature; washed (TBS-T) and mounted with coverslips (Fluoromont-G slide mounting medium, Electron Microscopy Sciences). Immmunofluorescence images were captured using a Nikon Eclipse E400 microscope and the NIS-2000 Elements v 2.0 software (Nikon). All images were artificially colored, resized, and merged using Adobe Photoshop CS3 software (Adobe).

Immunohistochemical analysis of patient lymphoma samples

Tissue microarrays (TMAs) were constructed by using duplicate 0.6-mm cores from diagnostic (Arthur et al., 2018) and analyzed by immunohistochemistry using standard protocols (Dominguez-Sola and Cattoretti, 2017). Briefly, heat-induced epitope retrieval was performed in EDTA buffer (pH9.0) for phospho-AKT S473 or Citrate buffer (pH6.0) for FOXO1, followed by blocking endogenous peroxidase activity in PBS plus 3% H2O2. Phospho-AKT S473 staining was performed manually using a rabbit monoclonal anti-pAKT S473 antibody (Dako #M3628), by overnight incubation at 4°C. After several washes, slides were incubated with an anti-Rabbit-HRP polymer secondary antibody (Rabbit Envision, Dako, Denmark) and developed using amino-ethyl-carbazole (AEC) as substrate (AEC kit, Vector Labs). FOXO1 staining was performed on the Ventana platform (Roche, Basel, Switzerland) using routine staining protocols (Arthur et al., 2018). All slides stained for both markers were reviewed and scored by an expert hematopathologist (P.F.).

Scoring

Both p-AKT and FOXO1 histoscores were defined as the product of intensity (1-3) and percentage of positive cells (0%–100%). The final histoscore ranged from 0 to 300, with negative cases having no signal or very low (< 20) histoscores. For FOXO1, both nuclear and cytoplasmic scores were annotated. The final designation into nuclear, nuclear-cytoplasmic or cytoplasmic was generated upon clustering all cases according to the ratio between nuclear and cytoplasmic scores. Briefly, the log10 value of the nuclear score was divided by the log10 value of the cytoplasmic score and used to annotate the cases as 'cytoplasmic' (ratio < 0.5), 'nucleo-cytoplasmic' (ratio 0.5-1.5) or 'nuclear' (ratio > 1.5).

Immunohistochemical analysis of mouse lymphoid tissues and quantitative studies

Immunohistochemical analyses of FFPE mouse tissues was performed as previously reported (Dominguez-Sola and Cattoretti, 2017), with minor modifications. Briefly, we prepared FFPE tissue blocks after overnight fixation with 10% buffered formalin at room temperature, then quick washes in distilled water and incubation in 70% ethanol (overnight) prior to paraffin embedding and tissue block preparation. All FFPE sections were dewaxed and rehydrated all paraffin sections and treated with heat-induced epitope retrieval with citrate buffer (pH 6.0) plus 0.5% Tween. We blocked endogenous peroxidase activity and biotin (when required, using Avidin-Biotin blocking kit, VectorLabs) and then in PBS containing 0.1%Tween, 3% BSA and 5% goat serum (Jackson ImmunoResearch). Each section was then incubated with specific primary antibodies (from different species when combining two makers, e.g., Ki67+B220 or CD21+PNA) diluted in SignalStain antibody diluent (Cell Signaling Technologies) overnight at 4°C, in a

humid chamber. After several washes (TBS+0.1%Tween), we incubated the sections with species-specific secondary antibodies conjugated to HRP (SignalStain Boost IHC Detection Reagent, Cell Signaling Technologies) or biotin (anti-Rat) for 45 min at room temperature, and developed immune complexes using AEC substrate (AEC staining kit, Sigma-Aldrich) or Vectastain ABC kit and Vector Blue AP substrate (Vector Labs). IHC image acquisition was performed using a whole slide scanner (Nanozoomer S60, Hamamatsu Photonics) at 40X magnification. Details on all antibodies and kits is provided in the Key resources table.

Quantification and Image Analysis of GCs:

Image analysis was performed using the open-source software QuPath (Bankhead et al., 2017). We use tissue annotation features to define the region of interest (ROI) and to measure the whole section and germinal center areas (magic wand feature), as highlighted by BCL6 expression. Only germinal centers with regular shape and with clusters of > 20 B cells were included in the analysis. We measured an average of 30 germinal centers per mouse (range 15-38). Number and size of germinal centers were determined using the annotation measurement tool. Size of GC was expressed as square pixel size (px^2) and both GC number and size were expressed relative to the total area of each corresponding section. Measurements above or below 3 standard deviations away from the mean value were considered outliers and excluded from the analysis.

RNA isolation and quality control

SUDHL4 cells were resuspended in IMDM+10%FBS at 0.5×10^6 cells/mL and incubated for 12 h prior to harvesting for gene expression analyses. We then washed the cells once in cold PBS and lysed in 500 uL TRIzol Reagent (Thermo Fisher Scientific). RNA isolation was immediately performed using standard protocols and chloroform extraction. The top (aqueous) phase was transferred to a new tube, and an equal volume of cold 100% Ethanol was added. This mix was loaded into an RNase easy column (PureLink RNA Mini kit, ThermoFisher Scientific) for RNA isolation extraction and eluted with RNase-free water. RNA concentration was measured in a NanoDrop spectrophotometer and RNA integrity determined in Agilent Bioanalyzer.

RT-qPCR

cDNA was synthesized from total RNA using the SuperScript IV VILO kit (Thermofisher Scientific). For RT-qPCR, we used 10 ng of cDNA per reaction and various primer combinations (in triplicate) mixed in 2x SYBR PCR mastermix (Bimake). Quantitative PCR was performed in a Bio-Rad CFX384 Real-Time PCR Detection System. Results were calculated using the ($2^{-\Delta\Delta CT}$) method, normalizing to TBP and POL2RA. Primer sequences are listed in the Key resources table.

Gene expression analyses by RNA-sequencing

To generate libraries for RNA-seq we used total RNA (300ng) with a RIN score > 8 was and the Nugen Universal Plus mRNA-seq kit (NuGen). Libraries were multiplexed and sequenced on an Illumina NextSeq to a minimum of 25 million single-end reads. Fastq reads were aligned to human genome reference hg19 using TopHat (Trapnell et al., 2009) with options –read-mismatches 2 –read-edit-dist 2 –max-multihits 10. We used Cufflinks (Trapnell et al., 2010) to assign alignments to genes and generate normalized fpkm values, which we used for principle component analysis and unsupervised hierarchical clustering using GenePattern (Reich et al., 2006). To generate raw read counts from BAM alignment files we used Htseq-count (Anders et al., 2015). Read counts were used as input for differential expression analysis using DESEQ2 (Love et al., 2014). Genes were considered to be differentially expressed if they had a q-value below 0.05. The significant genes from DESEQ2 were used to run pathway enrichment analyses using the Molecular Signatures Database (MSigDB) from the Broad Institute.

For *Gene Set Enrichment Analysis* (GSEA v4.0) (Subramanian et al., 2005), raw counts from RNA-seq data were first normalized using the *VoomNormalize* (v2) module (Law et al., 2014) in GenePattern, with default parameters. We then used the normalized data as input to run GSEA with 'Enrichment Statistic' -weighted and 'Metric for Ranking Genes' -Diff_of_classes.

Chromatin immunoprecipitation sequencing (ChIP-seq)

For this assay, we used starved cells. Briefly, SUDHL4 cells (10^7) were washed twice with Hanks' Buffered Saline Solution (HBSS), then resuspended in HBSS with 1% IMDM and incubated at 37C for 3 h. Cells were then harvested, washed once in PBS and resuspended in 20 mL of PBS with 1% formaldehyde and incubated for 15 min at room temperature with gentle agitation. Crosslinks were quenched with 0.125M glycine for 5 min, washed cells twice with ice cold PBS with protease and phosphatase inhibitors, then transferred to a DNA/protein lo-bind Eppendorf tube. Nuclei were then isolated by resuspending the cell pellet in a buffer containing 10mM Tris pH 8.0, 10 mM NaCl, and 0.2% NP-40 and incubating on ice for 30 min. Nuclei were pelleted by centrifugation at 7400 rpm, 4°C for 30 s. The nuclear pellet was resuspended in a buffer containing 50 mM Tris pH 8.0, 10 mM EDTA, and 1% SDS and left on ice for 30 min with gentle vortexing every 5 min. Each sample was then transferred to a 1.5 mL sonication microtube (Diagenode) and sonicated at low-power setting on a Diagenode Bioruptor (Diagenode) until chromatin fragments were 200-600 bp on average.

250 ug of chromatin were diluted (1:4) in IP dilution buffer containing 20 mM Tris pH 8.0, 2 mM EDTA, 150 mM NaCl, 1% Triton X-100, and 0.01% SDS, and precleared by incubation with Magna ChIP protein A+G Dynabeads (Millipore Sigma 16-663) pre-coated with ChIP-grade rabbit IgG (Abcam #37415), for 3 h at 4C. The diluted chromatin was then separated from the beads using a magnet and transferred to a new tube. We reserved 10% of the pre-cleared, sonicated chromatin as "input," stored at −80C. To the rest of the sample, we added 5 ug of FOXO1 ChIP-seq grade antibody (Abcam #39670) and all tubes were incubated rotating overnight at 4°C. We added Magna ChIP protein A+G beads and incubated, while rotating, for an additional 3 h at 4°C. We washed the beads with

buffers of increasing stringency, resuspended the beads in DNA elution buffer containing 1% SDS and 0.1M NaHCO₃, and incubated, shaking for 1 h at 65°C. We transferred the supernatant containing DNA-immunocomplexes into a new tube and reversed crosslinks by incubating overnight at 65°C in the presence of NaCl and RNase. The entire sample of ChIP DNA and 10 ng of input DNA were used to synthesize libraries using the NEBNext NGS DNA Library Preparation kit (New England Biolabs cat #E7645 and #E7500), according to manufacturer's instructions.

ChIP-seq data analysis

Before aligning and analyzing the ChIP-seq data, we combined the reads from technical duplicates. We aligned reads to the UCSC hg19 genome using Bowtie2 (Langmead and Salzberg, 2012), allowing for 2 mismatches. After removing duplicates using SAMtools (Li et al., 2009), all samples had a minimum of 25 million uniquely mapped reads. Peak calling was done in MACS2 (Zhang et al., 2008) over the input at a threshold of FDR < 0.05. We used HOMER (Heinz et al., 2010) *mergePeaks* with default function to find shared and differential peaks between samples. Peaks overlapping between SUDHL4-M1L clone #39 and SUDHL4-M1L clone #47 were deemed as shared "M1L peaks" and used in the comparison with those found in WT SUDHL4 samples. All heatmaps and read density plots were generated with Deeptools2.0 (Ramírez et al., 2016) *computeMatrix* and *plotHeatmap* functions. For *de novo* motif discovery, we used the HOMER *findMotifs* function selecting a 150 bp region around the peak center; and the *annotatepeaks* function for peak annotation.

FOXO1 luciferase reporter assays

The FOXO1 reporter construct contains a tandem of three Daf-16 binding elements (DBE), 5′CATTTGTT3′ or 5′GTAAACAA3′ separated by a 4bp stuffer (5′CTAT3′); as previously described (Furuyama et al., 2000; Zanella et al., 2009). The DBE core sequence differs from the 5′CAAAACA3′ core sequence in the insulin-responsive element (IRE) and is recognized by all FOXO proteins with higher affinity than IREs (Obsil and Obsilova, 2011). We subcloned the 3x DBE tandem via Gibson assembly into pNL3.1, which encodes for Nanoluc (Nluc) luciferase (Promega #N1031) driven by a minimal promoter. We also generated control, mutated constructs based containing a 3x tandem of mutated DBE sites (5′GTAAGCAA3′) as in previous reports (Tsai et al., 2007). All reporter assays were performed by transient co-transfection of HEK293T cells with pcDNA3-FOXO1 (wild-type or variants), pNL3.1-3xDBE (or mutant version) and a pGL4.26 control reporter (Firefly Luciferase), using polyethylenimine (PEI). Cells were maintained in DMEM+1% serum throughout the experiment and lysed at 48h post-transfection. Reporter activity was measured using Nano-Glo Dual-Luciferase Reporter Assay System (Promega, #N1610). Relative reporter activity was calculated by normalizing Nanoluc reporter levels to Firefly control and the activity of the DBE mutant reporter, which controlled for effects unrelated to the target DBE sequence.

Gene knockdown experiments

shRNAs were designed using the splash algorithm (Pelossof et al., 2017) and subcloned into the RT3-REVIR backbone (Fellmann et al., 2013) via Gibson Assembly (New England Biolabs) using the restriction sites EcoRI/XhoI. All shRNA-RT3-REVIR constructs and packaging vectors were transiently transfected in HEK293T cells to generate lentiviral particles, which were used to transduce lymphoma cell lines at high multiplicity of infection. Stably transduced cell pools were expanded under antibiotic selection (puromycin). shRNA expression was induced by adding 1.5 ug/mL doxycycline to the culture medium, and cells were harvested and lysed in denaturing conditions and presence of protease and phosphatase inhibitor cocktails (Pierce/ThermoFisher, #88669), 72h post-induction.

Isolation of light (LZ) and dark zone (DZ) germinal center B cells from human tonsils

Tonsils were processed by mechanical disruption of the tissue and cells were isolated using Ficoll-Paque PLUS (#45-001-749, Fisher Scientific) by gradient centrifugation. LZ and DZ human tonsillar GC fractions were sorted from mononuclear cell suspensions as previously detailed, using a combination of magnetic and fluorescence-activated cell sorting (Victora et al., 2012). Cell suspensions were kept on ice at all times in PBS+0.5% BSA supplemented with phosphatase inhibitor cocktail, and LZ and DZ fractions sorted into cold PBS-0.5% BSA. Purity of each fraction was confirmed to be > 95%.

Primary lymphoma tumor datasets

We compiled RNA-seq, whole-exome sequencing and survival data of two separate large primary DLBCL case series previously reported by Staudt and cols. and Morin, Scott and cols. The first dataset (Schmitz et al., 2018) (n = 481 cases) is stored at the dbGaP repository (the Database of Genotypes and Phenotypes), dbGaP accession number (phs001444; Genomic Variation in Diffuse Large B cell Lymphomas), and was accessed under project #20252. The second dataset, from British Columbia Cancer (BCC) had been previously detailed in Arthur et al. (2018) and Ennishi et al. (2019) is stored at the European Genome-phenome Archive (https://ega-archive.org), EGAS00001002657. Access was provided by D. Scott. This dataset comprises 347 primary cases. These datasets were available in the form of alignment files (BAM format). Raw gene expression counts were calculated using *featureCounts* 1.6.3 (Liao et al., 2014) using the BAM files as input; and subsequently normalized to transcripts per million (TPM).

Survival Analysis: Survival analyses were completed using the 'survival' package available in R. Kaplan-Meier curves were generated with the *ggsurvplot* function included in the *survminer* R package (Kassambara et al., 2017; see Key resources table).

Leading Edge Meta-analysis and case stratification

Leading Edge Meta-analysis (LEM) was performed as previously described, with minor modifications (Godec et al., 2016; Reese et al., 2016; Tan et al., 2016). Briefly, we used Gene Set Enrichment Analysis (GSEA) (Subramanian et al., 2005) to compile a list of signatures enriched with FDR < 25% in each phenotype (wild-type or FOXO1 mutant SUDHL4) from a total of 456 signatures related to immune responses and B cells (see Table S4). Using the *Leading-Edge Analysis* tool in the GSEA package, we generated a 'W' matrix of "leading edges" including all those genes responsible for the enrichment of each signature in each phenotype (704 genes and 52 signatures; see Table S4). We loaded this matrix as input in the "Leading Edge Metanalysis" pipeline, publicly available in the Github repository (https://github.com/lamarck2008/LEM). The code in original pipeline was updated with minor modifications to run with Python3. The updated pipeline is available upon request. LEM was run with options -n 100 -s 2 -e 5 for step 1, -r 4 for step 2, and a cutoff of 3 for step 4. LEM uses non-negative matrix factorization (NMF) to identify a small number of co-regulated groups of genes ('metagenes'), which are a biologically meaningful representation of the original gene sets (Tan et al., 2016). LEM of the 52 input leading edges identified a total of 6 metagenes (4+2) (Table S4; Figure 8). We then used single-sample GSEA (Barbie et al., 2009) to calculate the enrichment score of each metagene in a set of 138+ GCB-like DLBCL selected from two primary DLBCL datasets (Arthur et al., 2018; Ennishi et al., 2019; Schmitz et al., 2018), using log2(TPM+1) normalized RNA-seq data. The *ssGSEAProjection* (v4) tool is available at the GenePattern server (Reich et al., 2006). *ssGSEAProjection* was used with default parameters, no sample normalization. This produced a projection matrix with scores for each metagene/sample pair. We then used Consensus Clustering (Monti et al., 2003) to discover sample clusters based on the activity of the LEM metagenes (*ConsensusClustering* tool, GenePattern Server. Parameters: kmax = 7, 2000 resampling iterations, hierarchical clustering by columns, Euclidean correlation, average linkage, row-column normalization - 1000 iterations). This analysis resolved the dataset in two clusters for best fit (k = 2).

QUANTIFICATION AND STATISTICAL ANALYSIS

All statistical analyses were performed by using GraphPad Prism Software (version 6 or 8). We used statistical tests appropriate for each experimental setup, with at least 3 independent experiments with multiple biological replicates (isogenic clones or single mice). Details for number of experiments, biological replicates, dispersion and precision measures, as well as each statistical test used are detailed in the corresponding figure legends. Sample size for animal experiments was determined with G*Power software (80% Power, alpha 0.5). Significance levels are reported as *p < 0.05; **p < 0.01, ***p < 0.001.